

Fixing Overconfidence in Dynamic Neural Networks

Lassi Meronen^{1,2}

Martin Trapp¹

Andrea Pilzer³

Le Yang⁴

Arno Solin¹

¹Aalto University

²Saab Finland Oy

³NVIDIA

⁴Xi'an Jiaotong University

{lassi.meronen, martin.trapp, arno.solin}@aalto.fi, apilzer@nvidia.com, yangle15@xjtu.edu.cn

Abstract

Dynamic neural networks are a recent technique that promises a remedy for the increasing size of modern deep learning models by dynamically adapting their computational cost to the difficulty of the inputs. In this way, the model can adjust to a limited computational budget. However, the poor quality of uncertainty estimates in deep learning models makes it difficult to distinguish between hard and easy samples. To address this challenge, we present a computationally efficient approach for post-hoc uncertainty quantification in dynamic neural networks. We show that adequately quantifying and accounting for both aleatoric and epistemic uncertainty through a probabilistic treatment of the last layers improves the predictive performance and aids decision-making when determining the computational budget. In the experiments, we show improvements on CIFAR-100, ImageNet, and Caltech-256 in terms of accuracy, capturing uncertainty, and calibration error.

1. Introduction

The ability to scale deep neural networks up to millions of parameters (e.g., [29, 44, 50]) on massive data sets (e.g., [8, 28]) has been a crucial part of achieving impressive performance, sometimes exceeding human experts on many natural-language processing and computer vision tasks. However, learning and deploying such models entails high computational costs and becomes increasingly difficult [44, 50], especially as inference costs arise for every deployed instance and can heavily add up [43].

Henceforth, there has been an increased interest in techniques for energy-efficient inference in deep learning [2, 13]. A particularly promising direction is to *dynamically* select the most cost-efficient sub-model based on the *difficulty* of the test sample. Dynamic neural networks (DNNs, [15, 18]) leverage a multi-exit architecture and *dynamically* route test samples based on their difficulty. For example, an image of a sunflower might be easy to classify, requiring less compute, while a tiger in a snowy environment might be more ambiguous and can only be correctly identified after

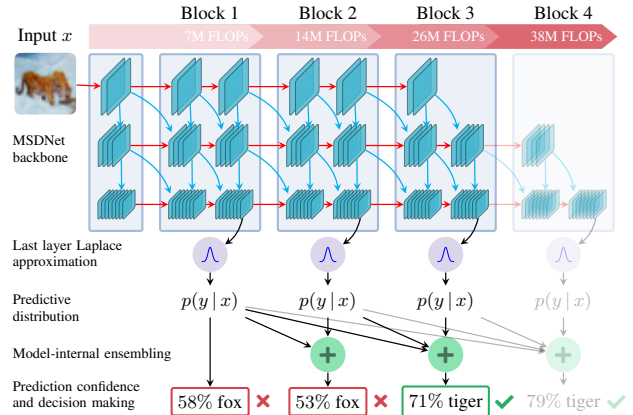


Figure 1. Increasing depth/scale of a dynamic neural network. Our probabilistic decision-making captures a calibrated confidence estimate, allowing better decisions from the intermediate classifiers on when to stop the evaluation (decision on whether to output the prediction is shown in red and green outline).

several stages (cf. Fig. 1). The adaptive early exiting is typically based on the confidence scores at the individual exits or learned gating functions [15]. Thus, it is crucial that the predictive densities or gating functions are robust and allow for trustworthy decision-making. However, current approaches are problematic as typical neural architectures are: (i) **miscalibrated** [14], (ii) **overconfident** [16], and (iii) their predictions do not capture **epistemic** uncertainties (uncertainty about the true model, see [22]).

Uncertainty quantification is the interest of probabilistic (or *Bayesian*) methods in deep learning. Bayesian deep learning [48] has recently gained increasing attention in the machine learning community as a means for uncertainty quantification (e.g., [22, 49]) and model selection (e.g., [3, 19]), compromising, among others, advancements on prior specification (e.g., [11, 34–36]) and efficient approximate inference schemes (e.g., [7, 25, 30]). Even though some of these advancements have recently found application in computer vision (e.g., [41, 45, 47]), they have not found adoption for decision-making in DNNs.

In this work, we propose a new probabilistic treatment of the multiple exits of DNNs by applying a Bayesian formula-

tion combined with efficient post-hoc approximate inference using multiple last-layer Laplace approximations [24]. Our probabilistic treatment reduces *overconfidence*, improves *calibration*, and captures *epistemic* uncertainties arising through the uncertainty about the true model without increasing the computational burden significantly. Moreover, we propose aggregating predictions across the exits to utilise uncertainties arising at earlier stages and show that accounting for uncertainties in decision-making (bottom in Fig. 1) outperforms the standard dynamic neural network (MSDNet [18]) on CIFAR-100, ImageNet, and Caltech-256.

Our contributions can be summarized as follows: (i) We introduce a probabilistic treatment for early exit dynamic neural networks (DNNs) utilising a Bayesian formulation. (ii) We present a computationally efficient post-hoc approach for uncertainty-aware decision-making by leveraging our efficient last-layer Laplace approximation implementation combined with model-internal ensembling, which works out of the box without retraining. (iii) Finally, we show on CIFAR-100, ImageNet, and Caltech-256 that our probabilistic treatment improves over a conventional approach in accuracy, capturing uncertainties, and calibration error.

1.1. Related work

Dynamic neural networks (DNNs, [15, 26, 42]) that utilise intermediate classifiers, allow early exit of easy samples during inference. This tailors the computation depth of each input sample at runtime and offers complementary performance gains to other efficiency optimisations. The early works developing the chain-structured models show limited performance due to the interference among different classifiers [21, 46], which is addressed by the proposed Multi-Scale DenseNet (MSDNet, [18]) via dense connections and a multi-scale structure. Moreover, the MSDNet is further improved from the aspects of reducing resolution redundancy [51] and training process [27, 39]. However, the confidence-based early exiting criterion applied in these aforementioned works can be problematic, and the generated confidence does not necessarily reflect the complexity of the input. Furthermore, the poor estimation of uncertainty in these models makes it difficult to decide which samples are easy and which are hard, and further vulnerable to the slow-down attacks in [17]. Despite these shortcomings, multi-exit models have been successfully applied for image segmentation [23], image caption prediction [10], and to natural language processing by implementing early exits into a BERT model [9, 43].

Bayesian deep learning [22, 37] allows including prior knowledge and assumptions into deep learning models, and formulates their predictions through a probabilistic treatment. Calculating the posterior distribution of a Bayesian neural network is usually intractable, and approximate inference techniques need to be used, such as variational inference [4], deep ensembles [25], MC dropout [12], or

Laplace approximation [20, 24, 40]—each having strengths and weaknesses. A key guiding principle in this work is constraining the computational budget, which leads us to propose an approach that utilizes computationally light Laplace approximations and re-uses predictions of DNN intermediate classifiers in a model-internal ensemble. Prior work does not consider the overconfidence or calibration of confidence estimates that DNNs use to make decisions on which samples require more computational budget.

2. Background

We are concerned with image classification under computational budget restrictions subject to a labelled training data set, $\mathcal{D}_{\text{train}} = \{\mathbf{x}_i, \mathbf{y}_i\}_{i=1}^{n_{\text{train}}}$, where \mathbf{x}_i is d -dimensional input (e.g., RGB image with $d = 3 \times N_{\text{pixels}}$). Labels \mathbf{y}_i are c -dimensional one-hot encoded vectors indicating the correct class label in the classification task. The computational budget restrictions are applied in the form of a budgeted batch classification setup, in which a fixed computational budget B —measured in average floating point operations per input sample (FLOPs)—must be distributed across a batch of test samples to achieve the highest possible accuracy. Here, a model is trained on the training set $\mathcal{D}_{\text{train}}$ with an ‘unlimited’ computational budget and tested on a set of test samples $\mathcal{D}_{\text{test}} = \{\mathbf{x}_j, \mathbf{y}_j\}_{j=1}^{n_{\text{test}}}$ using a *limited* average budget B per test sample.

For a DNN model having n_{block} intermediate classifiers (see Fig. 1 for a sketch), we refer to the predictive distribution of each of these classifiers as $p_k(\hat{\mathbf{y}}_i | \mathbf{x}_i)$, $k = 1, 2, \dots, n_{\text{block}}$. The feature representation before the last linear layer of each classifier is referred to as $\phi_{i,k} = f_k(\mathbf{x}_i)$, and the parameters of the last linear layer are $\theta_k = \{\mathbf{W}_k, \mathbf{b}_k\}$. The prediction $p_k(\hat{\mathbf{y}}_i | \mathbf{x}_i)$ is obtained from the feature representation $\phi_{i,k}$ as follows: $p_k(\hat{\mathbf{y}}_i | \mathbf{x}_i) = \text{softmax}(\hat{\mathbf{z}}_{i,k})$, where $\hat{\mathbf{z}}_{i,k} = \mathbf{W}_k \phi_{i,k} + \mathbf{b}_k$.

Our focus is on fixing the overconfidence of DNN architectures that dynamically adapt the network depth utilising early exiting by intermediate classifiers, each with increasing computational requirements. Implementing classifiers as early exits into a single network allows reusing computation and reduces the overall inference cost compared to using independent models of varying sizes. Early versions of such DNNs suffer from interference between classifiers during training [21, 46]. This problem can be alleviated by using dense connectivity between intermediate classifiers, and by utilising a multi-scale structure having fine and coarse-scale features throughout the network. This architecture is referred to as a Multi-Scale DenseNet (MSDNet, [18]), and we use it as a backbone to demonstrate our methods of improving uncertainty estimation, as at the time of writing it clearly outperforms other image classification DNNs that use intermediate classifiers. However, our methods are applicable to any DNN that utilises early exiting. Fig. 1 visualizes the structure

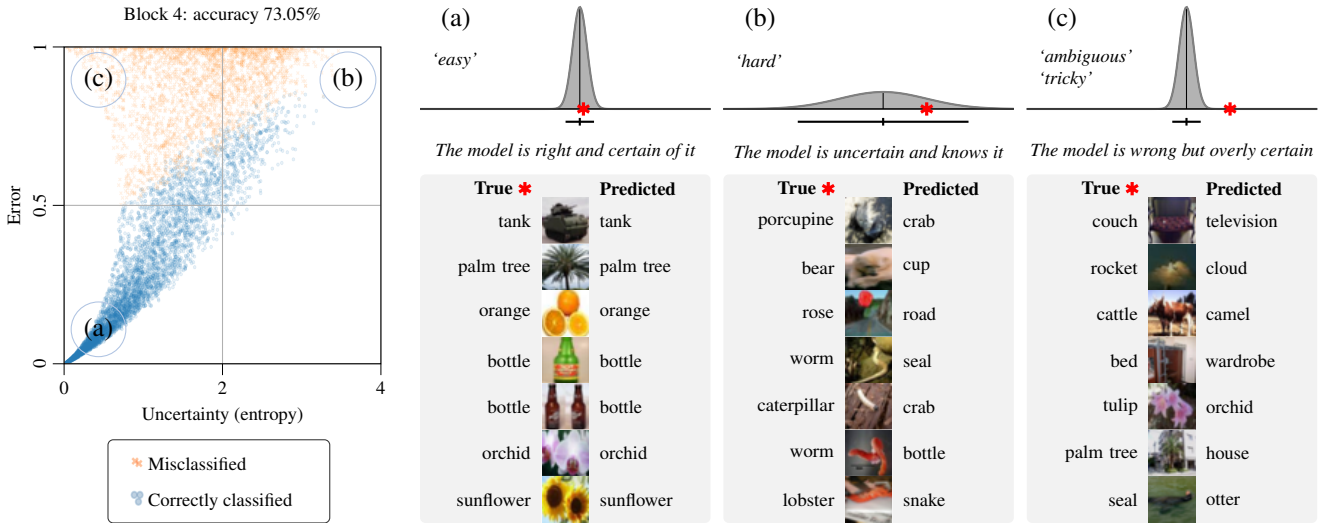


Figure 2. **Knowing what the model does not know.** An uncertainty–error scatter plot showing CIFAR-100 test set predictions for the last classifier of an MSDNet with Laplace and model-internal ensembling, and example images of three types corresponding to three areas in the uncertainty–error scatter plot. The error is defined as $1 - p(\hat{y} = y)$, where $p(\hat{y} = y)$ is the predicted probability on the correct label.

of the DNN backbone and the applied uncertainty quantification methods. The visualized FLOPs numbers are for the ‘small’ MSDNet model used for CIFAR-100 (see Sec. 4)

The challenge of efficiently using a DNN backbone with intermediate classifiers is the decision-making problem of when to exit the model. The goal is to use less capacity for clear ‘easy’ samples while unleashing more capacity for more difficult or tricky cases. To achieve this goal, the model must be well-calibrated and know when it is uncertain about its predictions. Many DNN models (e.g. [18, 46]) use predicted confidences from intermediate classifiers to make decisions on early exiting, but the calibration of these predictions is not controlled.

Uncertainty estimation in deep learning is often divided into estimating two different types of uncertainty [22]: *aleatoric* and *epistemic*. Aleatoric uncertainty is related to randomness intrinsic to the task at hand and cannot be reduced. Epistemic uncertainty is related to our knowledge of the task and can be reduced by learning more about the task, e.g., by obtaining more data. In our problem setting of image classification, epistemic uncertainty is related to the model parameters. In Fig. 2, epistemic uncertainty is present in the predictions for images of type (b): the model has not learned the task well enough to classify these difficult sample images correctly. On the other hand, an example of aleatoric uncertainty is seen in some of the sample images of type (c): an image may contain objects from multiple classes, and the most prominent object is not necessarily labelled as the correct class (‘ambiguous’), or some images may be completely mislabelled. We refer to this kind of samples as ‘tricky’.

A Bayesian treatment to uncertainty estimation means

that instead of obtaining a single point estimate of the model parameters θ as the result of neural network training, Bayesian inference is used to obtain a *posterior distribution* over the model parameters given the training data $\mathcal{D}_{\text{train}}$:

$$p(\theta | \mathcal{D}_{\text{train}}) = \frac{p(\mathcal{D}_{\text{train}} | \theta) p(\theta)}{\int_{\theta} p(\mathcal{D}_{\text{train}}, \theta) d\theta} = \frac{[\text{likelihood}] \times [\text{prior}]}{[\text{model evidence}]}. \quad (1)$$

Usually, calculating the exact posterior for a deep learning model is intractable. This means that the posterior of the model parameters must be approximated. One approach is to consider the $L - 1$ first layers of a deep neural network with L layers as a fixed feature extractor and limit the Bayesian treatment to the last (L^{th}) layer. This drastically decreases the number of parameters for which the posterior distribution needs to be estimated. However, computations are usually still infeasible as no analytic solution exists, and further approximations are needed.

An efficient approximation to the posterior of the model parameters is the Laplace approximation, which performs a second-order Taylor expansion of Eq. (1) around the maximum *a posteriori* (MAP) estimate of the target distribution, resulting in a Gaussian distribution. The model parameters representing the MAP estimate can be found by maximising the unnormalised posterior: $p(\theta | \mathcal{D}) \propto p(\mathcal{D}_{\text{train}} | \theta) p(\theta) = p(\theta, \mathcal{D})$, which is commonly assumed in log-space for numerical stability: $\log p(\theta, \mathcal{D}_{\text{train}}) = \log p(\mathcal{D}_{\text{train}} | \theta) + \log p(\theta)$. In classification tasks, we typically minimise the cross-entropy loss, which is equivalent to maximising the log-likelihood. Moreover, commonly used regularisation methods such as weight decay can be interpreted as a log-prior. Hence, deep learning models

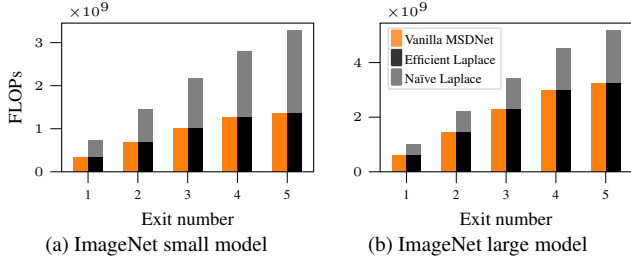


Figure 3. Test time computational cost of ■ naïve and ■ efficient methods of sampling the Laplace predictive distribution (50 MC samples) compared against the ■ vanilla MSDNet, on ImageNet data. Results shown for each intermediate exit. Details in App. C.

learned with conventional training methods for classification tasks can be seen as maximising the unnormalised log-posterior and we, therefore, **directly obtain the MAP estimate** (θ_{MAP}) required for Laplace approximations through standard training. The Laplace approximation of the posterior is then formed using a multivariate Gaussian centred at the MAP estimate with covariance given by the inverse of the Hessian \mathbf{H} of the negative log-posterior, *i.e.*, $N(\theta_{\text{MAP}} | \mathbf{H}^{-1})$ and $\mathbf{H} := -\nabla_{\theta}^2 \log p(\theta | \mathcal{D}) |_{\theta_{\text{MAP}}}$. The Hessian can be efficiently approximated using the generalised Gauss-Newton algorithm [5] or by Kronecker factorisation [33, 40].

3. Methods

Our aim is to couple an early exit DNN backbone with an uncertainty-aware decision-making process. For uncertainty quantification, we leverage the early exit structure of the DNN architecture and propose an approach that uses Laplace approximations and model-internal ensembling. The motivation for improving uncertainty estimation is that if the intermediate classifiers in the DNN can more accurately estimate the uncertainty in their predictions, they can better recognise which samples are hard and require further computation, and for which samples the prediction is already confident enough to be exited early.

3.1. Laplace approximation of a dynamic NN

To approximate the predictive posterior we propose an efficient implementation of a last-layer Laplace approximation for each intermediate classifier of the DNN. Using our computationally cheap last-layer approach enables us to stay resource-efficient while at the same time improving the decision-making within DNNs. Note that in this section we have dropped the index k for the intermediate exit for simplicity, as all operations are done independently for each exit.

To save on computational costs of sampling from a larger dimensional Gaussian on the last-layer parameters $N(\theta_{\text{MAP}}, \mathbf{H}^{-1})$, where $\theta_{\text{MAP}} = \{\mathbf{W}_{\text{MAP}}, \mathbf{b}_{\text{MAP}}\}$ are the last-layer MAP parameters of one exit, we linearly project the Gaussian to a predictive distribution $p(\hat{\mathbf{z}}_i | \mathbf{x}_i)$. This directly allows us to sample pre-softmax outputs $\hat{\mathbf{z}}_i$

and reduces the dimensionality of the Gaussian to the number of classes c . The final prediction $\hat{\mathbf{y}}_i$ is then calculated by sampling n_{MC} samples from the predictive Gaussian: $\hat{\mathbf{y}}_i = \frac{1}{n_{\text{MC}}} \sum_{l=1}^{n_{\text{MC}}} \text{softmax}(\hat{\mathbf{z}}_i^{(l)})$. If performed naïvely [24], this forces performing all sampling-related computation at test time, resulting in a per sample cost of $\text{FLOPs}_{\text{naïve}} = 2c^2(n_{\text{MC}} + 1) + \frac{1}{3}c^3 + 2p^2 + p - 1$ which grows cubically with the number of classes c (p is the feature space dimensionality: $\phi_i \in \mathbb{R}^p$). Absorbing the last layer biases into the weight matrix allows us to shift most of the computation required for sampling to be performed before test time. The resulting efficient Laplace implementation for DNNs has a cost of $\text{FLOPs}_{\text{efficient}} = 2cn_{\text{MC}} + 2p^2 + 5p + 2$, making Laplace approximation computationally viable in the budget restricted regime. Fig. 3 shows a computational cost comparison for the naïve and efficient Laplace approximations. More detailed analysis is presented in App. C.

Applying a Laplace approximation only to the last linear layer at each intermediate exit now provides us with a Gaussian distribution $p(\hat{\mathbf{z}}_i | \mathbf{x}_i) = N(\hat{\mathbf{W}}_{\text{MAP}}^{\top} \hat{\phi}_i, (\hat{\phi}_i^{\top} \mathbf{V} \hat{\phi}_i) \mathbf{U})$ for each classifier. Here $\mathbf{V}^{-1} \otimes \mathbf{U}^{-1} = \mathbf{H}^{-1}$ is an approximate inverse Hessian, being a Kronecker factorisation of the generalised Gauss-Newton matrix and $\hat{\phi}_i = (\phi_i^{\top}, 1)^{\top}$ are the features after augmenting the biases into the weights. Samples from this distributions are calculated as $\hat{\mathbf{z}}_i^{(l)} = \hat{\mathbf{W}}_{\text{MAP}}^{\top} \hat{\phi}_i + (\hat{\phi}_i^{\top} \mathbf{V} \hat{\phi}_i)^{\frac{1}{2}} (\mathbf{L} \mathbf{g}^{(l)})$, where $\mathbf{g}^{(l)} \sim N(\mathbf{0}, \mathbf{I})$ and \mathbf{L} is the Cholesky factor of \mathbf{U} .

To ensure well calibrated predictions from the Laplace approximation, it is useful to utilise temperature scaling [14] on the sampled predictions $\hat{\mathbf{y}}_i$. In practice, this means dividing each sampled pre-softmax output $\hat{\mathbf{z}}_i^{(l)}$ with a temperature scaling parameter T before taking the softmax. Also the Laplace prior variance σ is a hyperparameter affecting the results. We use a different value of T and σ for each classifier in the network. To choose appropriate values for the temperature scaling and prior variance parameters, we perform a grid search over possible pairs of values of T and σ , selecting the pair of values that minimises the negative log-predictive density score on the validation set for the classifier in question. Details on this grid search are in App. A.

3.2. Model-internal ensembling

To improve the predictive uncertainty and robustness of the DNN predictions, we utilise the idea of ensembling multiple predictions together [25]. However, using deep ensembles, where M independent networks are trained, is not feasible in the budget-restricted scenario. Instead, we utilise the predictions of intermediate classifiers in the dynamic neural network to form the ensemble and refer to this as a *model-internal ensemble* (MIE). The predictions from different intermediate classifiers are neither independent nor equal, as they are predictions from different stages of the same computational pipeline, and later classifiers have more

Samples in histogram (error > 0.5): Our model: 36.53%, Vanilla model: 33.33%

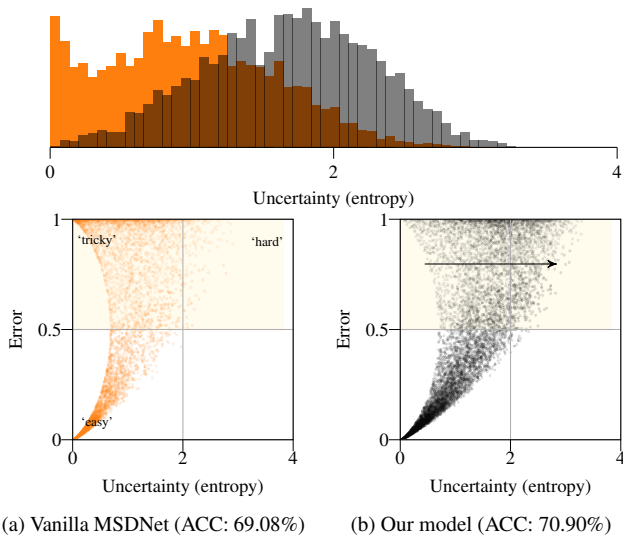


Figure 4. Comparison of uncertainty–error scatter plots from the **second to last classifier** of a vanilla MSDNet and our model with Laplace and model-internal ensembling. The uncertainty histogram on the top shows points with error > 0.5: the uncertainty should be high for the model to be able to recognize these samples as ‘hard’, and continue their evaluation to the next block. For our model these samples have a high uncertainty, while the vanilla MSDNet is overconfident. See Sec. 3.3 for definition of error.

capacity compared to earlier classifiers. To account for the difference in capacity in the MIE members, we can scale their influence to the final prediction in proportion to their computational complexity. Predictions from intermediate classifiers for forming an MIE are readily available and require no additional computation, as they need to be calculated to make the decision whether to continue computation further in the network. The model-internal ensemble prediction for the k^{th} classifier in an early exit DNN is:

$$p_k^{\text{ens}}(\hat{y}_i | \mathbf{x}_i) = \frac{1}{\sum_{l=1}^k w_l} \sum_{m=1}^k w_m p_m(\hat{y}_i | \mathbf{x}_i). \quad (2)$$

This is a weighted average of intermediate classifiers up to classifier k , for which we are calculating the MIE prediction. Later classifiers have more predictions in the average to aggregate, as more already calculated intermediate predictions are available. The weights w_m are the computational costs of the DNN in FLOPs up to classifier m . The added computational cost of MIE is marginal (see App. C for details).

3.3. Illustrating the intuition

Our model hinges on the realization that properly capturing epistemic uncertainty is key to making informed decisions. This is visible in Figs. 2 and 4 that demonstrate how better uncertainty quantification can improve the decision-making in a DNN. In Fig. 2, samples of type (c)

are ones that the model has predicted with high confidence, but the predicted label is incorrect. These can be mislabelled samples or samples that are very ambiguous. However, for a poorly calibrated model, the type (c) samples may also include a large number of samples that the model predicted overconfidently for no intuitive reason, and that should instead be of type (b): hard samples that the current stage of the model can’t accurately classify. This can be seen in Fig. 4 where the standard DNN model has a large number of overconfidently predicted samples in the upper left corner of the scatter plot. In this figure, we can see that the improved calibration of our model allows these samples to move to the upper right corner of the scatter plot. This change prevents these predictions from exiting at the current intermediate classifier and instead allows for potentially improving the prediction in the later steps of the DNN. In figures, the error is defined as $1 - p(\hat{y} = y)$, where $p(\hat{y} = y)$ is the predicted probability on the correct label.

For the decision-making to be efficient in a DNN, each intermediate classifier should have calibrated uncertainties and not show too many samples in the upper left area of the uncertainty–error scatter plots. Fig. 5 shows that this is true for our model, and the picture samples in Fig. 2 under the label (c) show that the samples remaining in the upper-left corner are mostly ambiguous samples, which even a calibrated model would predict incorrectly but confidently.

4. Experiments

We performed a series of experiments on benchmark image classification tasks to assess the improvements obtained through our probabilistic treatment applied to an early-exit DNN. For each model size for all data sets, a common backbone DNN (MSDNet [18]) was trained minimising the L2 regularised sum of cross-entropy losses computed for all exits on the training set. We trained three different-sized DNN backbone models on each data set to cover a larger range of budgets. Depending on the desired budget, only one of these models would be used at a time. We refer to these models as ‘small’, ‘medium’, and ‘large’.

After training, we evaluated each model on the test set in a budgeted batch classification setup. Early exiting decisions were based on model predicted confidence, for which thresholds $t_k, k = 1, 2, \dots, n_{\text{block}}$ were calculated on the validation set. We refer to [18] for details on the calculation of the thresholds. We report the Top-1 and Top-5 accuracies of each model over a range of computational budgets measured in average floating point operations (FLOPs) per test sample. In addition, following the recommendations for better validation metrics in image analysis [31], we compare the negative log-predictive density (NLPD) and the expected calibration error (ECE). Note that NLPD captures both accuracy and uncertainty quantification quality while ECE assesses only calibration, *i.e.*, how consistent the confidence

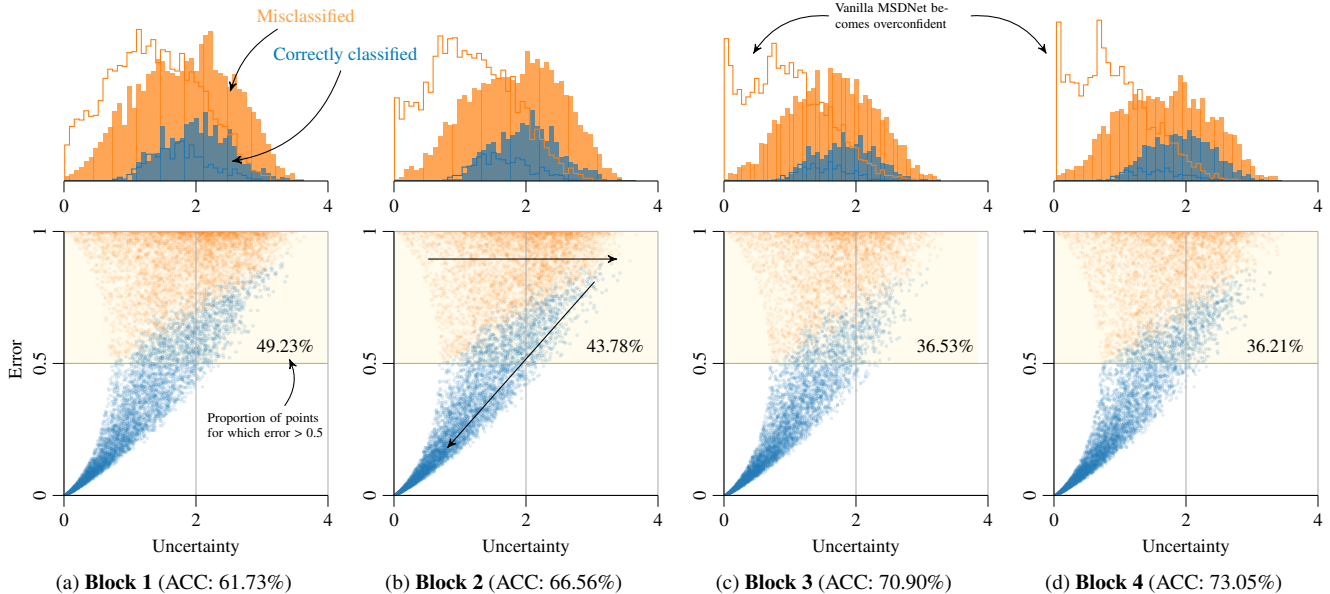


Figure 5. Model certainty grows with capacity. The bottom scatter plots show \bullet correctly classified and \ast misclassified test points on an uncertainty vs. error axis. The uncertainty of points in the top half is summarized as a histogram above each scatter plot (in scale with each other). Our model consistently adds capacity to calibrate itself to tricky cases (‘tricky’ \rightarrow ‘hard’) and improves accuracy (‘hard’ \rightarrow ‘easy’) over the blocks, while the vanilla MSDNet model (solid line in histograms, for reference) does not. Fig. 8 in App. B shows corresponding scatter plots for vanilla MSDNet, and uncertainty histograms including all points in the scatter plots for both models. See Sec. 3.3 for definition of error.

Table 1. Table of Top-1/Top-5 accuracy, negative log-predictive density (NLPD), and expected calibration error (ECE) for different models on CIFAR-100 and ImageNet data. All numbers are averages over a range of computational budgets in the budgeted batch classification setup. ‘MIE Laplace $T_{\text{opt}} \sigma_{\text{opt}}$ ’-model corresponds to ‘Our model’ that is referred to in other figures. MIE stands for model-internal ensembling.

$(n_{\text{train}}, d, c, n_{\text{batch}})$		CIFAR-100 (50000, 3072, 100, 64)				IMAGENET (1281167, 150528, 1000, 256)			
		Top-1 ACC \uparrow	Top-5 ACC \uparrow	NLPD \downarrow	ECE \downarrow	Top-1 ACC \uparrow	Top-5 ACC \uparrow	NLPD \downarrow	ECE \downarrow
Small	MSDNet (vanilla)	69.25	90.48	1.498	0.182	68.15	88.22	1.338	0.019
	+ Laplace $T_{\text{opt}} \sigma_{\text{opt}}$	69.06 -0.19	90.58 $+0.10$	1.208 -0.289	0.073 -0.109	68.10 -0.05	88.18 -0.04	1.337 -0.001	0.015 -0.005
	+ MIE	69.97 $+0.72$	90.88 $+0.40$	1.218 -0.280	0.080 -0.102	68.27 $+0.12$	88.13 -0.10	1.355 $+0.017$	0.055 $+0.036$
	+ MIE Laplace $T_{\text{opt}} \sigma_{\text{opt}}$	69.84 $+0.59$	91.09 $+0.61$	1.133 -0.364	0.017 -0.165	68.31 $+0.16$	88.11 -0.11	1.356 $+0.018$	0.052 $+0.032$
Medium	MSDNet (vanilla)	74.12	91.94	1.549	0.190	72.78	91.01	1.123	0.033
	+ Laplace $T_{\text{opt}} \sigma_{\text{opt}}$	73.92 -0.20	92.01 $+0.06$	1.070 -0.479	0.083 -0.107	72.72 -0.07	91.03 $+0.03$	1.118 -0.005	0.018 -0.015
	+ MIE	75.03 $+0.91$	92.97 $+1.03$	1.011 -0.538	0.050 -0.140	72.98 $+0.20$	91.12 $+0.11$	1.119 -0.004	0.042 $+0.009$
	+ MIE Laplace $T_{\text{opt}} \sigma_{\text{opt}}$	74.99 $+0.86$	93.23 $+1.29$	0.944 -0.605	0.026 -0.164	73.04 $+0.26$	90.96 -0.05	1.121 -0.002	0.031 -0.003
Large	MSDNet (vanilla)	75.36	92.78	1.475	0.178	74.33	91.57	1.066	0.050
	+ Laplace $T_{\text{opt}} \sigma_{\text{opt}}$	75.32 -0.05	92.83 $+0.05$	0.996 -0.479	0.075 -0.103	74.29 -0.04	91.53 -0.04	1.053 -0.013	0.020 -0.030
	+ MIE	76.32 $+0.95$	93.50 $+0.72$	0.949 -0.525	0.061 -0.117	74.82 $+0.49$	91.88 $+0.30$	1.029 -0.037	0.028 -0.022
	+ MIE Laplace $T_{\text{opt}} \sigma_{\text{opt}}$	76.34 $+0.98$	93.84 $+1.05$	0.885 -0.590	0.025 -0.152	74.80 $+0.47$	91.81 $+0.24$	1.032 -0.034	0.032 -0.019

scores are with the posterior probabilities. See App. A.5 for more details on the metrics. In figures, ‘Our model’ refers to an MSDNet backbone using Laplace approximation and MIE, while optimizing temperature scales and Laplace prior variances in a grid search. We additionally trained DenseNet and ResNet models as baselines, see App. A.4 for details on them. For more baseline results we refer to [18, Sec. 5.2].

Ablation studies were performed to investigate the individual contribution of the Laplace approximation and model-internal ensembling (MIE) to the model performance, testing models that use either only Laplace or only MIE. The results of this ablation study are included in Tab. 1 and Tab. 2. Re-

sults of a more comprehensive ablation study are in Tabs. 6 and 7 in App. B. Note that as Laplace and MIE are applied on the same trained vanilla MSDNet model that is used on its own, the differences in the results are not from randomness between different training runs. Laplace approximation improves the uncertainty quantification properties of the model by lowering NLPD and ECE values, whereas MIE usually improves both accuracy and uncertainty quantification properties. Considering overall performance over all four metrics (Top-1 and Top-5 accuracy, NLPD, and ECE), we can see that Laplace and MIE together give the best performance on CIFAR-100, whereas on ImageNet and Caltech-256 using MIE alone or together with Laplace both give roughly

Table 2. Table of Top-1/Top-5 accuracy, NLPD, and ECE for different models on Caltech-256 data. All numbers are averages over a range of computational budgets in the budgeted batch classification setup. ‘MIE Laplace $T_{\text{opt}} \sigma_{\text{opt}}$ ’-model corresponds to ‘Our model’ that is referred to in other figures.

		CALTECH-256 (25607, 150528, 257, 128)			
$(n_{\text{train}}, d, c, n_{\text{batch}})$		Top-1 ACC \uparrow	Top-5 ACC \uparrow	NLPD \downarrow	ECE \downarrow
Small	MSDNet (vanilla)	61.0	78.2	2.16	0.18
	+ Lap $T_{\text{opt}} \sigma_{\text{opt}}$	60.5 -0.5	78.1 -0.1	1.86 -0.29	0.05 -0.13
	+ MIE	61.9 $+0.9$	78.8 $+0.6$	1.94 -0.21	0.08 -0.10
	+ MIE Lap $T_{\text{opt}} \sigma_{\text{opt}}$	61.7 $+0.6$	79.0 $+0.8$	1.81 -0.34	0.09 -0.09
Medium	MSDNet (vanilla)	63.8	80.2	1.98	0.17
	+ Lap $T_{\text{opt}} \sigma_{\text{opt}}$	63.4 -0.4	79.9 -0.3	1.74 -0.24	0.07 -0.10
	+ MIE	65.1 $+1.3$	81.4 $+1.2$	1.72 -0.26	0.08 -0.09
	+ MIE Lap $T_{\text{opt}} \sigma_{\text{opt}}$	64.3 $+0.5$	81.3 $+1.1$	1.65 -0.33	0.08 -0.09
Large	MSDNet (vanilla)	64.9	80.7	1.90	0.16
	+ Lap $T_{\text{opt}} \sigma_{\text{opt}}$	64.7 -0.2	80.7 $+0.0$	1.65 -0.25	0.04 -0.12
	+ MIE	65.9 $+0.9$	82.4 $+1.8$	1.62 -0.28	0.06 -0.10
	+ MIE Lap $T_{\text{opt}} \sigma_{\text{opt}}$	65.6 $+0.7$	82.5 $+1.8$	1.58 -0.32	0.09 -0.07

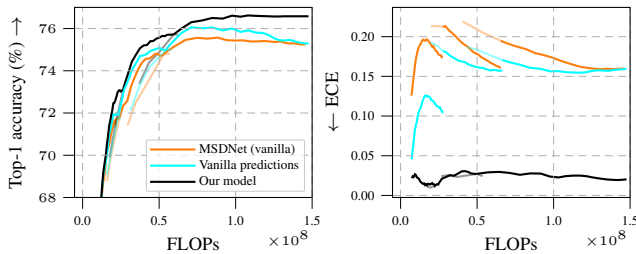


Figure 6. A decision-making experiment, where vanilla MSDNet and ‘Our model’ are compared to results obtained using our model for decision-making, and taking predictions from vanilla MSDNet (labelled ‘Vanilla predictions’). Full results in Fig. 9 in App. B.

equally good results. Despite some inconsistency in the combination of uncertainty quantification methods giving best performance, it is clear that improving uncertainty estimation improves the DNN performance over the vanilla model. The range of budgets over which results were averaged to obtain the numbers in Tabs. 1 and 2 are listed in Tab. 3 in App. A. **CIFAR-100** experiment results are visualized in Fig. 7 and numerical results are presented in Tab. 1. The three model sizes, small, medium, and large, are plotted as separate curves in Fig. 7. From the results in Fig. 7 we see that our model improves Top-1 and Top-5 accuracies over all tested computational budget levels, compared to the vanilla MSDNet model (in-line with results in [18]), and improves uncertainty quantification and calibration properties, which is seen in the decrease of negative log-predictive density (NLPD) and expected calibration error (ECE). From the curves, we can pinpoint at 10^8 FLOPs an improvement of 1.2 %-points in Top-1 accuracy and 1.1 %-points in Top-5 accuracy. We also note that although the vanilla MSDNet has clearly superior Top-1 accuracy compared to baseline ResNet and DenseNet models, it has poor performance in terms of NLPD and ECE in comparison to the baselines. CIFAR-100 experiment details are in App. A.1.

To investigate the contribution of better decision-making

on the improved predictive performance, we performed an experiment separating the improvement due to better decision-making from the improvement due to better predictions at individual intermediate exits. In this experiment, we replaced the vanilla model decision-making with the decision-making of our model, while using the vanilla model predictions for calculating the results. Results on CIFAR-100 are in Fig. 6 showing that our approach improves both decision-making (orange vs. light blue) and prediction quality (light blue vs. black). Interestingly, apart from improving accuracy, better decision-making also improves calibration, as seen from the improved ECE (details in App. B).

ImageNet experiment results are visualized in Fig. 7, and numerical results are presented in Tab. 1. Fig. 7 shows that on larger computational budgets, our model achieves improvements over the vanilla MSDNet model on all metrics. We note that the ECE numbers achieved by the vanilla MSDNet on ImageNet data are much better than those achieved by the vanilla MSDNet on CIFAR-100 data, suggesting relatively good calibration especially on lower budgets, and resulting in limited usefulness of uncertainty quantification methods. As the computational budget increases, vanilla MSDNet becomes less calibrated, negatively affecting the decision-making at the intermediate classifiers, which is seen in worse accuracy compared to our model. The good calibration of the vanilla MSDNet on ImageNet can be explained by the relatively small model size preventing overfitting the data. The largest MSDNet model used for ImageNet here has 62 million parameters, while the current state-of-the-art model [6] has 2440 million parameters. From the accuracy curves in Fig. 7 we can pinpoint at $2.5 \cdot 10^9$ FLOPs an improvement of 0.63 %-points in Top-1 accuracy and 0.34 %-points in Top-5 accuracy. ImageNet experiment details are in App. A.2.

Caltech-256 is an image classification data set with similar resolution images as ImageNet, but with a small number of training samples. For Caltech-256 the same backbone DNN models were used as for ImageNet. Results are visualized in Fig. 7 where we see similar trends as for CIFAR-100, with uncertainty quantification techniques improving performance on all metrics. Numerical results are presented in Tab. 2, where different uncertainty quantification methods excel at different metrics, but improve consistently over the vanilla MSDNet. We note that the same backbone DNNs that were used for ImageNet, benefit more from our uncertainty quantification methods when used on Caltech-256, possibly due to the smaller training set size that allows overfitting with these model sizes. We can deduce that uncertainty quantification in DNNs is beneficial especially when the standard model is overfitting the data, which is usually the case. From the accuracy curves in Fig. 7 we can pinpoint at $2.5 \cdot 10^9$ FLOPs an improvement of 1.4 %-points in Top-1 accuracy and 1.8 %-points in Top-5 accuracy. Caltech-256 experiment details are in App. A.3.

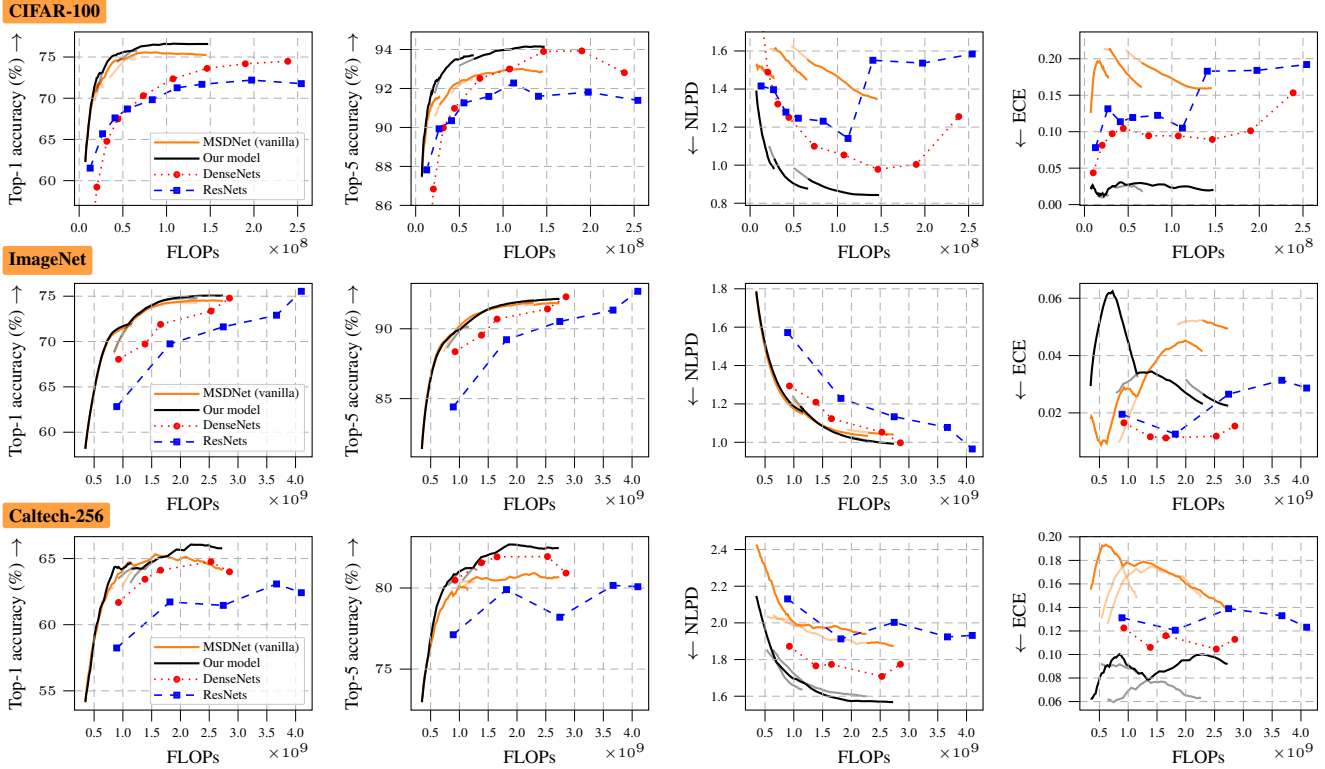


Figure 7. Accuracy (Top-1 & Top-5) and uncertainty metrics (NLPD and ECE) on a budgeted batch classification task as a function of average computational budget per image (FLOPs) on different data sets with a small/medium/large model, and ResNet/DenseNet baselines.

5. Conclusion and Discussion

We have demonstrated the importance of uncertainty quantification in dynamic neural networks (DNNs). For this purpose, we employed a probabilistic treatment of DNNs and leveraged a computationally efficient post-hoc posterior approximation through multiple last-layer Laplace approximations together with model-internal ensembling (MIE). Our approach substantially improves the internal decision-making process fundamental to DNNs, as evidenced by improved Top-1 and Top-5 accuracy, NLPD, and ECE on CIFAR-100, ImageNet, and Caltech-256. We found that uncertainty quantification and calibration are especially crucial for large-scale models that overfit training data—stressing their importance in DNNs applied to real-world scenarios.

Why Laplace and MIE? Uncertainty quantification comes in many facets and, if done in DNNs, has to be computationally efficient to be viable for budget-constrained applications. In this work, we proposed to employ last-layer Laplace approximations at each exit of the DNN. Although the Laplace approximation is a more crude approximation to the posterior in comparison to techniques such as deep ensembles, it provides a good trade-off between accuracy of the approximation and computational costs, which is essential to DNNs. In the experiments, we showed that our efficient Laplace approach adds little computational overhead and provides

overall NLPD and ECE improvements in most experiments. In addition, we showed that MIE can further boost performance with little additional costs by informing consecutive blocks in the DNN about the predictive uncertainties of previous exits. As a conclusion, the Laplace approximations account for epistemic uncertainties of each exit *independently* while MIE allows us to incorporate dependence between the exits—hence, complementary to each other.

Broader Impact. This work contributes towards improving the resource and energy efficiency of often prohibitively expensive deep learning models. For example, Microsoft reported [1] that answering Bing queries using BERT requires 2000 Azure GPU virtual machines to run in parallel. Uncertainty quantification is typically seen as a means of improving robustness and even safety of deep learning models, generally adding to the compute. This work takes the opposite direction leveraging uncertainty to reduce the overall number of floating point operations required for making predictions—while also providing more reliable uncertainty estimates for downstream applications. Improvements in DNNs allow using more powerful models in edge computing and on mobile hardware, and decreases the total energy usage of a heavy deep-learning task on non-constrained hardware.

The codes to replicate the results are available at <https://github.com/AaltoML/calibrated-dnn>.

References

- [1] Bing delivers its largest improvement in search experience using Azure GPUs. <https://tinyurl.com/tzhj3o8>. Accessed: 2022-11-11. [8](#)
- [2] Sergei Alyamkin, Matthew Ardi, Alexander C. Berg, Achille Brighton, Bo Chen, Yiran Chen, Hsin-Pai Cheng, Zichen Fan, Chen Feng, Bo Fu, Kent Gauen, Abhinav Goel, Alexander Goncharenko, Xuyang Guo, Soonhoi Ha, Andrew Howard, Xiao Hu, Yuanjun Huang, Donghyun Kang, Jaeyoun Kim, Jong-gook Ko, Alexander Kondratyev, Junhyeok Lee, Seungjae Lee, Suwoong Lee, Zichao Li, Zhiyu Liang, Juzheng Liu, Xin Liu, Yang Lu, Yung-Hsiang Lu, Deeptanshu Malik, Hong Hanh Nguyen, Eunbyung Park, Denis Repin, Liang Shen, Tao Sheng, Fei Sun, David Svitov, George K. Thiruvathukal, Baiwu Zhang, Jingchi Zhang, Xiaopeng Zhang, and Shaojie Zhuo. Low-power computer vision: Status, challenges, and opportunities. *IEEE Journal on Emerging and Selected Topics in Circuits and Systems*, 9(2):411–421, 2019. [1](#)
- [3] Javier Antorán, David Janz, James Urquhart Allingham, Erik A. Daxberger, Riccardo Barbano, Eric T. Nalisnick, and José Miguel Hernández-Lobato. Adapting the linearised laplace model evidence for modern deep learning. In *Proceedings of the International Conference on Machine Learning (ICML)*, volume 162 of *Proceedings of Machine Learning Research*, pages 796–821. PMLR, 2022. [1](#)
- [4] David M. Blei, Alp Kucukelbir, and Jon D. McAuliffe. Variational inference: A review for statisticians. *Journal of the American Statistical Association*, 112(518):859–877, 2017. [2](#)
- [5] Aleksandar Botev, Hippolyt Ritter, and David Barber. Practical Gauss-Newton optimisation for deep learning. In *Proceedings of the 34th International Conference on Machine Learning (ICML)*, volume 70 of *Proceedings of Machine Learning Research*, pages 557–565. PMLR, 2017. [4](#)
- [6] Xiangning Chen, Chen Liang, Da Huang, Esteban Real, Kaiyuan Wang, Yao Liu, Hieu Pham, Xuanyi Dong, Thang Luong, Cho-Jui Hsieh, et al. Symbolic discovery of optimization algorithms. *arXiv preprint arXiv:2302.06675*, 2023. [7](#)
- [7] Erik Daxberger, Agustinus Kristiadi, Alexander Immer, Runa Eschenhagen, Matthias Bauer, and Philipp Hennig. Laplace redux—Effortless Bayesian deep learning. In *Advances in Neural Information Processing Systems 34 (NeurIPS)*, pages 20089–20103. Curran Associates, Inc., 2021. [1](#)
- [8] Jia Deng, Wei Dong, Li-Jia Li, Kai Li, and Li Fei-Fei. Imagenet: A large-scale hierarchical image database. In *Proceedings of the IEEE/CVF Conference on Computer Vision and Pattern Recognition (CVPR)*, pages 248–255, 2009. [1](#)
- [9] Jacob Devlin, Ming-Wei Chang, Kenton Lee, and Kristina Toutanova. BERT: Pre-training of deep bidirectional transformers for language understanding. *arXiv preprint arXiv:1810.04805*, 2018. [2](#)
- [10] Zhongcong Fei, Xu Yan, Shuhui Wang, and Qi Tian. Deccap: Dynamic early exiting for efficient image captioning. In *Proceedings of the IEEE/CVF Conference on Computer Vision and Pattern Recognition (CVPR)*, pages 12206–12216. IEEE, 2022. [2](#)
- [11] Vincent Fortuin, Adrià Garriga-Alonso, Florian Wenzel, Gunnar Rätsch, Richard E. Turner, Mark van der Wilk, and Laurence Aitchison. Bayesian neural network priors revisited. In *Third Symposium on Advances in Approximate Bayesian Inference*, 2021. [1](#)
- [12] Yarin Gal and Zoubin Ghahramani. Dropout as a Bayesian approximation: Representing model uncertainty in deep learning. In *Proceedings of the International Conference on Machine Learning (ICML)*, volume 48 of *Proceedings of Machine Learning Research*, pages 1050–1059. PMLR, 2016. [2](#)
- [13] Abhinav Goel, Caleb Tung, Yung-Hsiang Lu, and George K. Thiruvathukal. A survey of methods for low-power deep learning and computer vision. In *Proceedings of the 6th IEEE World Forum on Internet of Things (WF-IoT)*, pages 1–6. IEEE, 2020. [1](#)
- [14] Chuan Guo, Geoff Pleiss, Yu Sun, and Kilian Q Weinberger. On calibration of modern neural networks. In *Proceedings of the 34th International Conference on Machine Learning (ICML)*, volume 70 of *Proceedings of Machine Learning Research*, pages 1321–1330. PMLR, 2017. [1](#), [4](#)
- [15] Yizeng Han, Gao Huang, Shiji Song, Le Yang, Honghui Wang, and Yulin Wang. Dynamic neural networks: A survey. *IEEE Transactions on Pattern Analysis and Machine Intelligence*, 44(11):7436–7456, 2022. [1](#), [2](#)
- [16] Matthias Hein, Maksym Andriushchenko, and Julian Bitterwolf. Why ReLU networks yield high-confidence predictions far away from the training data and how to mitigate the problem. In *Proceedings of the IEEE Conference on Computer Vision and Pattern Recognition (CVPR)*, pages 41–50, 2019. [1](#)
- [17] Sanghyun Hong, Yiğitcan Kaya, Ionuț-Vlad Modoranu, and Tudor Dumitraș. A panda? No, it’s a sloth: Slowdown attacks on adaptive multi-exit neural network inference. In *International Conference on Learning Representations (ICLR)*, 2020. [2](#)
- [18] Gao Huang, Danlu Chen, Tianhong Li, Felix Wu, Laurens van der Maaten, and Kilian Q. Weinberger. Multi-scale dense networks for resource efficient image classification. In *International Conference on Learning Representations (ICLR) Workshops*, 2018. [1](#), [2](#), [3](#), [5](#), [6](#), [7](#), [13](#)
- [19] Alexander Immer, Matthias Bauer, Vincent Fortuin, Gunnar Rätsch, and Mohammad Emtiyaz Khan. Scalable marginal likelihood estimation for model selection in deep learning. In *Proceedings of the International Conference on Machine Learning (ICML)*, volume 139 of *Proceedings of Machine Learning Research*, pages 4563–4573. PMLR, 2021. [1](#)
- [20] Alexander Immer, Maciej Korzepa, and Matthias Bauer. Improving predictions of Bayesian neural nets via local linearization. In *Proceedings of The 24th International Conference on Artificial Intelligence and Statistics (AISTATS)*, volume 130 of *Proceedings of Machine Learning Research*, pages 703–711. PMLR, 2021. [2](#)
- [21] Yiğitcan Kaya, Sanghyun Hong, and Tudor Dumitraș. Shallow-deep networks: Understanding and mitigating network overthinking. In *Proceedings of the 36th International Conference on Machine Learning (ICML)*, volume 97 of *Pro-*

- ceedings of Machine Learning Research*, pages 3301–3310. PMLR, 09–15 Jun 2019. **2**
- [22] Alex Kendall and Yarin Gal. What uncertainties do we need in Bayesian deep learning for computer vision? In *Advances in Neural Information Processing Systems 30 (NIPS)*, pages 5574–5584. Curran Associates, Inc., 2017. **1, 2, 3**
- [23] Alexandros Kouris, Stylianos I. Venieris, Stefanos Laskaridis, and Nicholas D. Lane. Multi-exit semantic segmentation networks. In *Proceedings of the 17th European Conference on Computer Vision (ECCV)*, volume 13681 of *Lecture Notes in Computer Science*, pages 330–349. Springer, 2022. **2**
- [24] Agustinus Kristiadi, Matthias Hein, and Philipp Hennig. Being Bayesian, even just a bit, fixes overconfidence in ReLU networks. In *Proceedings of the International Conference on Machine Learning (ICML)*, volume 119 of *Proceedings of Machine Learning Research*, pages 5436–5446. PMLR, 2020. **2, 4**
- [25] Balaji Lakshminarayanan, Alexander Pritzel, and Charles Blundell. Simple and scalable predictive uncertainty estimation using deep ensembles. In *Advances in Neural Information Processing Systems 30 (NIPS)*, pages 6402–6413. Curran Associates, Inc., 2017. **1, 2, 4**
- [26] Stefanos Laskaridis, Alexandros Kouris, and Nicholas D Lane. Adaptive inference through early-exit networks: Design, challenges and directions. In *Proceedings of the 5th International Workshop on Embedded and Mobile Deep Learning*, pages 1–6, 2021. **2**
- [27] Hao Li, Hong Zhang, Xiaojuan Qi, Ruigang Yang, and Gao Huang. Improved techniques for training adaptive deep networks. In *Proceedings of the IEEE/CVF International Conference on Computer Vision (ICCV)*, pages 1891–1900, 2019. **2**
- [28] Tsung-Yi Lin, Michael Maire, Serge J. Belongie, James Hays, Pietro Perona, Deva Ramanan, Piotr Dollár, and C. Lawrence Zitnick. Microsoft COCO: Common objects in context. In *Proceedings of the 13th European Conference on Computer Vision (ECCV)*, volume 8693 of *Lecture Notes in Computer Science*, pages 740–755. Springer, 2014. **1**
- [29] Ze Liu, Yutong Lin, Yue Cao, Han Hu, Yixuan Wei, Zheng Zhang, Stephen Lin, and Baining Guo. Swin transformer: Hierarchical vision transformer using shifted windows. In *Proceedings of the IEEE/CVF International Conference on Computer Vision (ICCV)*, pages 9992–10002. IEEE, 2021. **1**
- [30] Wesley J Maddox, Pavel Izmailov, Timur Garipov, Dmitry P Vetrov, and Andrew Gordon Wilson. A simple baseline for Bayesian uncertainty in deep learning. In *Advances in Neural Information Processing Systems 32 (NeurIPS)*, pages 13132–13143. Curran Associates, Inc., 2019. **1**
- [31] Lena Maier-Hein, Annika Reinke, Evangelia Christodoulou, Ben Glocker, Patrick Godau, Fabian Isensee, Jens Kleesiek, Michal Kozubek, Mauricio Reyes, Michael A. Riegler, Manuel Wiesenfarth, Michael Baumgartner, Matthias Eisenmann, Doreen Heckmann-Nötzel, A. Emre Kavur, Tim Rüd-sch, Minu Dietlinde Tizabi, Laura Ación, Michela Antonelli, Tal Arbel, Spyridon Bakas, Peter Bankhead, Arriel Benis, M. Jorge Cardoso, Veronika Cheplygina, Beth Cimini, Gary S. Collins, Keyvan Farahani, Bram van Ginneken, Daniel A. Hashimoto, Michael M. Hoffman, Merel Huisman, Pierre Jan-nin, Charles E. Kahn, Alexandros Karargyris, Alan Karthike-salingam, Hannes Kennigott, Annette Kopp-Schneider, Anna Kreshuk, Tahsin M. Kurç, Bennett A. Landman, Geert Litjens, Amin Madani, Klaus H. Maier-Hein, Anne L. Martel, Peter Mattson, Erik Meijering, Bjoern H. Menze, David Moher, Karel G. M. Moons, Henning Müller, Felix Nickel, Bren-nan Nichyporuk, Jens Petersen, Nasir Rajpoot, Nicola Rieke, Julio Saez-Rodriguez, Clarisa Sánchez Gutiérrez, Shravya Shetty, Maarten van Smeden, Carole H. Sudre, Ronald M. Summers, Abdel A. Taha, Sotirios A. Tsaftaris, Ben Van Cal-ster, Gaël Varoquaux, and Paul F. Jäger. Metrics reloaded: Pitfalls and recommendations for image analysis validation. *arXiv preprint arXiv:2206.01653*, 2022. **5**
- [32] TorchVision maintainers and contributors. Torchvision: Py-torch’s computer vision library. <https://github.com/pytorch/vision>, 2016. **13**
- [33] James Martens and Roger Grosse. Optimizing neural net-works with Kronecker-factored approximate curvature. In *Proceedings of the 32nd International Conference on Ma-chine Learning (ICML)*, volume 37 of *Proceedings of Ma-chine Learning Research*, pages 2408–2417. PMLR, 2015. **4**
- [34] Lassi Meronen, Christabella Irwanto, and Arno Solin. Sta-tionary activations for uncertainty calibration in deep learning. In *Advances in Neural Information Processing Systems 33 (NeurIPS)*, pages 2338–2350. Curran Associates, Inc., 2020. **1**
- [35] Lassi Meronen, Martin Trapp, and Arno Solin. Periodic activation functions induce stationarity. In *Advances in Neural Information Processing Systems 34 (NeurIPS)*, pages 1673–1685. Curran Associates, Inc., 2021. **1**
- [36] Eric Nalisnick, Akihiro Matsukawa, Yee Whye Teh, Dilan Gorur, and Balaji Lakshminarayanan. Do deep generative models know what they don’t know? In *International Con-ference on Learning Representations (ICLR)*, 2019. **1**
- [37] Radford M Neal. *Bayesian Learning for Neural Networks*. PhD thesis, University of Toronto, Toronto, Canada, 1995. **2**
- [38] Adam Paszke, Sam Gross, Francisco Massa, Adam Lerer, James Bradbury, Gregory Chanan, Trevor Killeen, Zeming Lin, Natalia Gimelshein, Luca Antiga, Alban Desmaison, Andreas Kopf, Edward Yang, Zachary DeVito, Martin Rai-son, Alykhan Tejani, Sasank Chilamkurthy, Benoit Steiner, Lu Fang, Junjie Bai, and Soumith Chintala. Pytorch: An imperative style, high-performance deep learning library. In *Advances in Neural Information Processing Systems 32 (NeurIPS)*, pages 8024–8035. Curran Associates, Inc., 2019. **12**
- [39] Mary Phuong and Christoph H Lampert. Distillation-based training for multi-exit architectures. In *Proceedings of the IEEE/CVF International Conference on Computer Vision (ICCV)*, pages 1355–1364, 2019. **2**
- [40] Hippolyt Ritter, Aleksandar Botev, and David Barber. A scalable Laplace approximation for neural networks. In *International Conference on Learning Representations (ICLR)*, 2018. **2, 4**
- [41] Subhankar Roy, Martin Trapp, Andrea Pilzer, Juho Kannala, Nicu Sebe, Elisa Ricci, and Arno Solin. Uncertainty-guided

- source-free domain adaptation. In *Proceedings of the 17th European Conference on Computer Vision (ECCV)*, volume 13685 of *Lecture Notes in Computer Science*, pages 537–555. Springer, 2022. **1**
- [42] Simone Scardapane, Michele Scarpiniti, Enzo Baccarelli, and Aurelio Uncini. Why should we add early exits to neural networks? *Cognitive Computation*, 12(5):954–966, 2020. **2**
- [43] Roy Schwartz, Gabriel Stanovsky, Swabha Swayamdipta, Jesse Dodge, and Noah A. Smith. The right tool for the job: Matching model and instance complexities. In *Proceedings of the 58th Annual Meeting of the Association for Computational Linguistics (ACL)*, pages 6640–6651. Association for Computational Linguistics, 2020. **1, 2**
- [44] Emma Strubell, Ananya Ganesh, and Andrew McCallum. Energy and policy considerations for deep learning in NLP. In *Proceedings of the 57th Conference of the Association for Computational Linguistics (ACL)*, pages 3645–3650. Association for Computational Linguistics, 2019. **1**
- [45] Yihong Sun, Adam Kortylewski, and Alan L. Yuille. Amodal segmentation through out-of-task and out-of-distribution generalization with a Bayesian model. In *Proceedings of the IEEE/CVF Conference on Computer Vision and Pattern Recognition (CVPR)*, pages 1205–1214. IEEE, 2022. **1**
- [46] Surat Teerapittayanon, Bradley McDanel, and Hsiang-Tsung Kung. Branchynet: Fast inference via early exiting from deep neural networks. In *International Conference on Pattern Recognition (ICPR)*, pages 2464–2469. IEEE, 2016. **2, 3**
- [47] Jianfeng Wang and Thomas Lukasiewicz. Rethinking bayesian deep learning methods for semi-supervised volumetric medical image segmentation. In *Proceedings of the IEEE/CVF Conference on Computer Vision and Pattern Recognition (CVPR)*, pages 182–190. IEEE, 2022. **1**
- [48] Andrew Gordon Wilson. The case for Bayesian deep learning. <https://cims.nyu.edu/~andrewgw/caseforbdl.pdf>, 2019. Technical Report. **1**
- [49] Andrew Gordon Wilson and Pavel Izmailov. Bayesian deep learning and a probabilistic perspective of generalization. In *Advances in Neural Information Processing Systems 33 (NeurIPS)*, pages 4697–4708. Curran Associates, Inc., 2020. **1**
- [50] Xiaowei Xu, Yukun Ding, Sharon Xiaobo Hu, Michael Niemier, Jason Cong, Yu Hu, and Yiyu Shi. Scaling for edge inference of deep neural networks. *Nature Electronics*, 1(4):216–222, 2018. **1**
- [51] Le Yang, Yizeng Han, Xi Chen, Shiji Song, Jifeng Dai, and Gao Huang. Resolution adaptive networks for efficient inference. In *Proceedings of the IEEE/CVF Conference on Computer Vision and Pattern Recognition (CVPR)*, pages 2369–2378, 2020. **2**

A. Experiment Details

In each experiment, the MSDNet backbone models are trained on the training data to minimise the L2 regularised sum of cross-entropy losses computed for all exits of the model. The L2 regularisation is implicit through weight decay in the SGD optimizer, and the loss for a single input sample is $\mathcal{L}_i = \sum_{k=1}^{n_{\text{block}}} -\ln p_k(\hat{y}_i = y_i | \mathbf{x}_i)$, where $p_k(\hat{y}_i = y_i | \mathbf{x}_i)$ is the predicted softmax confidence on the correct label y_i at classifier k . Moreover, validation data is used after every epoch to assess the performance of the model. Subsequently, we select the model that achieved the highest Top-1 accuracy on the validation set at the last classifier as the final model.

After training, we evaluate each model using the test set on a budgeted batch classification setup. For this, the computational budget is fixed, and each model must aim to classify the test set samples within the given budget. To achieve this, we use the validation set to calculate thresholds $t_k, k = 1, 2, \dots, n_{\text{block}}$, one for each exit, such that the overall cost of classifying all test samples does not exceed the predefined budget B in expectation. To utilise the thresholds t_k , we need to employ a metric of uncertainty assigned to each prediction. If the uncertainty does not exceed the pre-calculated threshold at stage k we exit the model at the current stage and otherwise pass the test sample to the next block and continue with the computation. In our experiments, this uncertainty metric is the prediction confidence: the maximum softmax output value for each sample in the case of a vanilla MSDNet. For our model leveraging Laplace approximations we compute the maximum of the predictive posterior probabilities. As increasing prediction confidence corresponds to decreasing uncertainty, a sample is exited at exit k if the predicted confidence exceeds the confidence threshold t_k that has been calculated on the validation set.

A grid search is used to select values for the temperature scaling hyperparameter T_k and Laplace approximation prior variance σ_k . The values of T_k used in the grid search for all models are the following: [0.3, 0.5, 0.7, 1.0, 1.3, 1.5, 1.7, 2.0, 2.5, 3.0]. The values of Laplace prior variance σ_k used in the grid search are [0.5, 0.7, 1.0, 1.3, 1.5, 1.7, 2.0, 2.5, 3.0, 4.0]. If the temperature scale or Laplace prior variance are not optimised for in a grid search, as in many ablation study model options, they are set to their default values of 1.0 and 2.0 respectively. When MIE is not used, the grid search for T_k and σ_k is performed independently for each exit k minimising the NLPD on the validation set. When using MIE, T_k and σ_k are optimised one exit at a time sequentially, starting from the first exit, minimizing the ensemble prediction NLPD. When performing the grid search for exit j , the already optimised values of T_k and σ_k for exits $k = 1 \dots j - 1$ remain fixed, and the values T_j and σ_j are optimised by selecting the pair of values that minimises the MIE prediction NLPD for exit j .

To obtain the numbers in Tabs. 1, 2, 6 and 7, results for each model over a range of budgets are averaged. The budget range is different for ImageNet/Caltech-256 and CIFAR-100 models, and for each of the small, medium, and large size models. The computational budget ranges for averaging results for each model are listed in Tab. 3. All experiments are implemented with PyTorch [38].

A.1. CIFAR-100 Model and Training Details

The CIFAR-100 training set of 50,000 images is split into 45,000 training images and 5,000 validation images. The test set has 10,000 images. On CIFAR-100, models are trained for 300 epochs using a batch size of 64 images, and the learning rate is initially set to 0.1 and is decayed to one-tenth at epochs 150 and 225. The optimiser is SGD with a momentum of 0.9 and weight decay of 10^{-4} . The MSDNet backbone of all CIFAR-100 models has three scales of features. The number of channels after the first layer is 16, and the number of channels added by each layer is 6.

On CIFAR-100 the ‘small’, ‘medium’, and ‘large’ DNN backbones have 4, 6, and 8 blocks and classifiers each, respectively. The small architecture has a total of 10 layers, and transition layers that reduce the number of scales by one are performed at layers 5 and 9. The medium architecture has a total of 21 layers, and transition layers are performed at layers 8 and 15. The large architecture has a total of 36 layers, with transition layers performed at layers 13 and 25. Tab. 4 shows more detailed information separately for each block of the small, medium, and large models.

A.2. ImageNet Model and Training Details

The ImageNet training set of 1,281,167 images is split into 1,231,167 training images and 50,000 validation images. The test set is the standard test set of 50,000 images. In preprocessing, the sample images that are of varying resolutions are resized to a resolution of 224 by 224 pixels. On ImageNet, models are trained for 90 epochs using a batch size of 256, and the learning rate is initially set to 0.1 and it

Table 3. Ranges of computational budgets (FLOPs) over which results are averaged for different models to obtain the results shown in Tabs. 1, 2, 6 and 7.

CIFAR-100		
Model size	Lower budget limit	Upper budget limit
Small	$7.0 \cdot 10^6$	$2.6 \cdot 10^7$
Medium	$2.5 \cdot 10^7$	$0.6 \cdot 10^8$
Large	$0.5 \cdot 10^8$	$1.4 \cdot 10^8$
ImageNet and Caltech-256		
Model size	Lower budget limit	Upper budget limit
Small	$3.5 \cdot 10^8$	$1.1 \cdot 10^9$
Medium	$7.5 \cdot 10^8$	$2.2 \cdot 10^9$
Large	$1.5 \cdot 10^9$	$2.6 \cdot 10^9$

Table 4. Additional details on the different MSDNet backbone architectures used for different model sizes on CIFAR-100, ImageNet, and Caltech-256. Each row in the table shows details of a specific block in the architecture. L is the number of layers, FLOPs is the computational cost of processing one input sample, and n_{params} is the number of model parameters. FLOPs and n_{params} are cumulative numbers *i.e.* they include the numbers from the previous blocks. This means that the cost for the entire architecture is the cost shown for the last block.

CIFAR-100			Small			Medium			Large		
Block number	L	FLOPs (10^6)	n_{params} (10^6)	L	FLOPs (10^6)	n_{params} (10^6)	L	FLOPs (10^6)	n_{params} (10^6)		
1	1	6.86	0.30	1	6.86	0.30	1	6.86	0.30		
2	2	14.35	0.65	2	14.35	0.65	2	14.35	0.65		
3	3	26.13	1.02	3	27.29	1.11	3	27.29	1.11		
4	4	38.04	1.42	4	46.56	1.61	4	48.45	1.73		
5	-	-	-	5	67.43	2.11	5	81.57	2.39		
6	-	-	-	6	89.09	2.85	6	112.64	3.18		
7	-	-	-	-	-	-	7	152.92	4.10		
8	-	-	-	-	-	-	8	192.69	5.31		

ImageNet			Small			Medium			Large		
Block number	L	FLOPs (10^6)	n_{params} (10^6)	L	FLOPs (10^6)	n_{params} (10^6)	L	FLOPs (10^6)	n_{params} (10^6)		
1	4	339.90	4.24	6	514.66	7.08	7	615.6	8.76		
2	4	685.46	8.77	6	1171.18	15.69	7	1436.39	20.15		
3	4	1008.16	13.07	6	1844.52	24.01	7	2283.21	31.73		
4	4	1254.47	16.75	6	2501.40	42.19	7	2967.42	41.86		
5	4	1360.53	23.96	6	2742.06	56.53	7	3253.79	62.31		

Caltech-256			Small			Medium			Large		
Block number	L	FLOPs (10^6)	n_{params} (10^6)	L	FLOPs (10^6)	n_{params} (10^6)	L	FLOPs (10^6)	n_{params} (10^6)		
1	4	339.62	3.95	6	514.28	6.70	7	615.26	8.33		
2	4	684.88	8.20	6	1170.40	14.90	7	1435.49	19.25		
3	4	1007.32	12.24	6	1843.36	22.86	7	2281.85	30.37		
4	4	1253.41	15.69	6	2499.59	40.38	7	2965.67	40.11		
5	4	1359.05	22.48	6	2739.66	54.13	7	3251.32	59.84		

is decayed to one-tenth at epochs 30 and 60. The optimiser is SGD with a momentum of 0.9 and weight decay of 10^{-4} . The MSDNet backbone of all ImageNet models has four scales of features and five blocks. The number of channels after the first layer is 32, and the number of channels added by each layer is 16.

The small, medium, and large models for ImageNet have five blocks and five classifiers each, but vary in the number of layers in each block (model architecture design follows [18]). The small architecture has a total of 20 layers, and transition layers that reduce the number of scales by one are performed at layers 6, 11, and 16. The medium architecture has a total of 30 layers, and transition layers are performed at layers 9, 17, and 25. The large architecture has a total of 35 layers, with transition layers at layers 10, 19, and 28. Tab. 4 shows more detailed information separately for each block of the small, medium, and large models.

A.3. Caltech-256 Model and Training Details

The Caltech-256 data set of 30,607 images is split to a training set of 23,107, a validation set of 2,500, and a test set of 5,000 samples. In preprocessing, the sample images that are of varying resolutions are resized to a resolution of 224 by 224 pixels, the same as for ImageNet data. The Caltech-256 data set has images from 257 categories.

On Caltech-256 the MSDNet backbone models are the same as for ImageNet, with the difference of the output dimensionality being 257 instead of 1,000, which affects

the number of parameters and FLOPs slightly. Caltech-256 models are trained for 180 epochs with a batch size of 128. This difference in training compared to ImageNet models is due to the smaller number of training samples and the smaller number of classes. The learning rate is initially set to 0.1 and is decayed to one-tenth at epochs 90 and 135. Apart from the mentioned differences, the Caltech-256 models are trained the same as the ImageNet models.

A.4. Details on Baseline Models and Their Training

We use ResNet and DenseNet models as baseline architectures for CIFAR-100, ImageNet, and Caltech-256 experiments. Tab. 5 shows the model architecture details for all the used baseline models. Both ResNet and DenseNet models are implemented using the implementations from Torchvision [32]. All ResNet models are built using the basic residual layer with two consecutive 3 by 3 convolutions, except for the ImageNet/Caltech-256 ResNet50, which uses the bottleneck residual layer. For ImageNet and Caltech-256 DenseNet models, the growth rate is 32 and the number of initial features is 64. For CIFAR-100 DenseNet models, the growth rate is 12 and the number of initial features is 24. For ImageNet and Caltech-256, the Torchvision implementations are used as they are. On Caltech-256 the baseline models are the same as for ImageNet, with the difference of the output dimensionality being 257, which affects the number of parameters and FLOPs slightly.

For CIFAR-100, the architectures need some modifica-

Table 5. Details of the baseline ResNet and DenseNet models that are shown for comparison in Fig. 7. FLOPs is the computational cost of processing one input sample, and n_{params} is the number of model parameters. L_{B_i} is the number of layers in block i of the model (a block here refers to all layers between transition layers that change the feature map size). For CIFAR-100 models $i = 1 \dots 3$ and for ImageNet models $i = 1 \dots 4$.

CIFAR-100 baseline models					
Model name	FLOPs	n_{params}	L_{B1}	L_{B2}	L_{B3}
ResNet8	$12.6 \cdot 10^6$	$8.39 \cdot 10^4$	1	1	1
ResNet14	$26.8 \cdot 10^6$	$18.1 \cdot 10^4$	2	2	2
ResNet20	$41.0 \cdot 10^6$	$27.8 \cdot 10^4$	3	3	3
ResNet26	$55.2 \cdot 10^6$	$37.6 \cdot 10^4$	4	4	4
ResNet38	$83.7 \cdot 10^6$	$57.0 \cdot 10^4$	6	6	6
ResNet50	$112 \cdot 10^6$	$76.4 \cdot 10^4$	8	8	8
ResNet62	$141 \cdot 10^6$	$95.9 \cdot 10^4$	10	10	10
ResNet86	$197 \cdot 10^6$	$135 \cdot 10^4$	14	14	14
ResNet110	$254 \cdot 10^6$	$174 \cdot 10^4$	18	18	18
DenseNet10	$10.0 \cdot 10^6$	$2.34 \cdot 10^4$	1	1	1
DenseNet16	$20.3 \cdot 10^6$	$4.88 \cdot 10^4$	2	2	2
DenseNet22	$31.7 \cdot 10^6$	$7.80 \cdot 10^4$	3	3	3
DenseNet28	$44.4 \cdot 10^6$	$11.1 \cdot 10^4$	4	4	4
DenseNet40	$73.4 \cdot 10^6$	$18.8 \cdot 10^4$	6	6	6
DenseNet52	$107 \cdot 10^6$	$28.0 \cdot 10^4$	8	8	8
DenseNet64	$146 \cdot 10^6$	$38.8 \cdot 10^4$	10	10	10
DenseNet76	$190 \cdot 10^6$	$51.0 \cdot 10^4$	12	12	12
DenseNet88	$239 \cdot 10^6$	$64.8 \cdot 10^4$	14	14	14

ImageNet baseline models						
Model name	FLOPs	n_{params}	L_{B1}	L_{B2}	L_{B3}	L_{B4}
ResNet10	$8.93 \cdot 10^8$	$5.42 \cdot 10^6$	1	1	1	1
ResNet18	$18.2 \cdot 10^8$	$11.7 \cdot 10^6$	2	2	2	2
ResNet26	$27.4 \cdot 10^8$	$18.0 \cdot 10^6$	3	3	3	3
ResNet34	$36.7 \cdot 10^8$	$21.8 \cdot 10^6$	3	4	6	3
ResNet50	$41.0 \cdot 10^8$	$25.6 \cdot 10^6$	3	4	6	3
DenseNet57	$9.24 \cdot 10^8$	$2.44 \cdot 10^6$	2	6	10	8
DenseNet65	$13.8 \cdot 10^8$	$2.93 \cdot 10^6$	4	6	12	8
DenseNet81	$16.5 \cdot 10^8$	$4.18 \cdot 10^6$	4	8	16	10
DenseNet97	$25.3 \cdot 10^8$	$5.44 \cdot 10^6$	6	12	16	12
DenseNet121	$28.5 \cdot 10^8$	$7.98 \cdot 10^6$	6	12	24	16

Caltech-256 baseline models						
Model name	FLOPs	n_{params}	L_{B1}	L_{B2}	L_{B3}	L_{B4}
ResNet10	$8.92 \cdot 10^8$	$5.04 \cdot 10^6$	1	1	1	1
ResNet18	$18.2 \cdot 10^8$	$11.3 \cdot 10^6$	2	2	2	2
ResNet26	$27.4 \cdot 10^8$	$17.6 \cdot 10^6$	3	3	3	3
ResNet34	$36.7 \cdot 10^8$	$21.4 \cdot 10^6$	3	4	6	3
ResNet50	$41.0 \cdot 10^8$	$24.0 \cdot 10^6$	3	4	6	3
DenseNet57	$9.24 \cdot 10^8$	$2.08 \cdot 10^6$	2	6	10	8
DenseNet65	$13.8 \cdot 10^8$	$2.55 \cdot 10^6$	4	6	12	8
DenseNet81	$16.5 \cdot 10^8$	$3.69 \cdot 10^6$	4	8	16	10
DenseNet97	$25.3 \cdot 10^8$	$4.87 \cdot 10^6$	6	12	16	12
DenseNet121	$28.5 \cdot 10^8$	$7.22 \cdot 10^6$	6	12	24	16

tions due to the smaller input dimensionality. For CIFAR-100 ResNets, the first convolutional layer is replaced by a 3 by 3 convolution with stride 1 and 16 output channels, and the max pooling layers are removed. For CIFAR-100 DenseNets, the first convolutional layer is replaced by a 3 by 3 convolution with stride 1, and the first batch normalization, max pooling, and ReLU operations are removed.

On CIFAR-100, ResNet and DenseNet models are trained for 300 epochs, and the learning rate is initially set to 0.1 and is decayed to one-tenth at epochs 150 and 225. On ImageNet, the ResNet and DenseNet models are trained for 90 epochs,

and the learning rate is initially set to 0.1 and it is decayed to one-tenth at epochs 30 and 60. On Caltech-256 the baseline models are trained for 180 epochs with a batch size of 128. The learning rate is initially set to 0.1 and is decayed to one-tenth at epochs 90 and 135. For all data sets all ResNet and DenseNet models use the SGD optimiser with a momentum of 0.9 and weight decay of 10^{-4} .

A.5. Details on the Used Performance Metrics

For reporting model performances, we use the Top-1 and Top-5 accuracies, the negative log-predictive density (NLPD), and the expected calibration error (ECE). Top-1 accuracy is the standard accuracy metric, and is the percentage of test predictions for which the highest model predicted probability was on the correct class. Top-5 accuracy is the percentage of test predictions, for which the correct class is among the five classes that the model assigned the highest probability. Negative log-predictive density (NLPD) is defined as:

$$\text{NLPD} = - \sum_{i=1}^{n_{\text{test}}} \log p(\hat{y}_i = y_i | \mathbf{x}_i), \quad (3)$$

where $p(\hat{y}_i = y_i | \mathbf{x}_i)$ is the model predicted probability on the correct label y_i . NLPD is a metric that captures both the quality of uncertainty estimates as well as the correctness of the predictions, most heavily penalizing overconfident incorrect predictions.

Expected calibration error (ECE) is defined as:

$$\text{ECE} = \sum_{j=1}^m b_j \| (p_j - \mu_j) \|, \quad (4)$$

where b_j is the fraction of test samples in bin $j = 1, \dots, m$, p_j is the Top-1 accuracy of the j^{th} bin, and μ_j is the average confidence of the predictions in the bin. We use $m = 10$ in our experiments. ECE assesses the calibration of each model, *i.e.*, how consistent the confidence scores are with the posterior probabilities.

B. Additional Results

Fig. 8 repeats the results from Fig. 5 and additionally shows corresponding scatter plots for the vanilla MSDNet for comparison. The bottom row in Fig. 8 shows predictive uncertainty histograms for all samples in the CIFAR-100 test set, comparing the vanilla MSDNet model to our model. The results are obtained using the small CIFAR-100 model. Comparing the scatter plots of our model with those of the vanilla model, we see that the vanilla model has more points in the top left corner of the plots, representing overconfident incorrect predictions. Looking at the bottom row histograms, we observe that the predictions from the vanilla MSDNet are overall more confident than those of our model.

Tab. 6 shows an extended version of the ablation study seen in Tab. 1, adding model versions that use Laplace approximation, but optimise only temperature scaling or

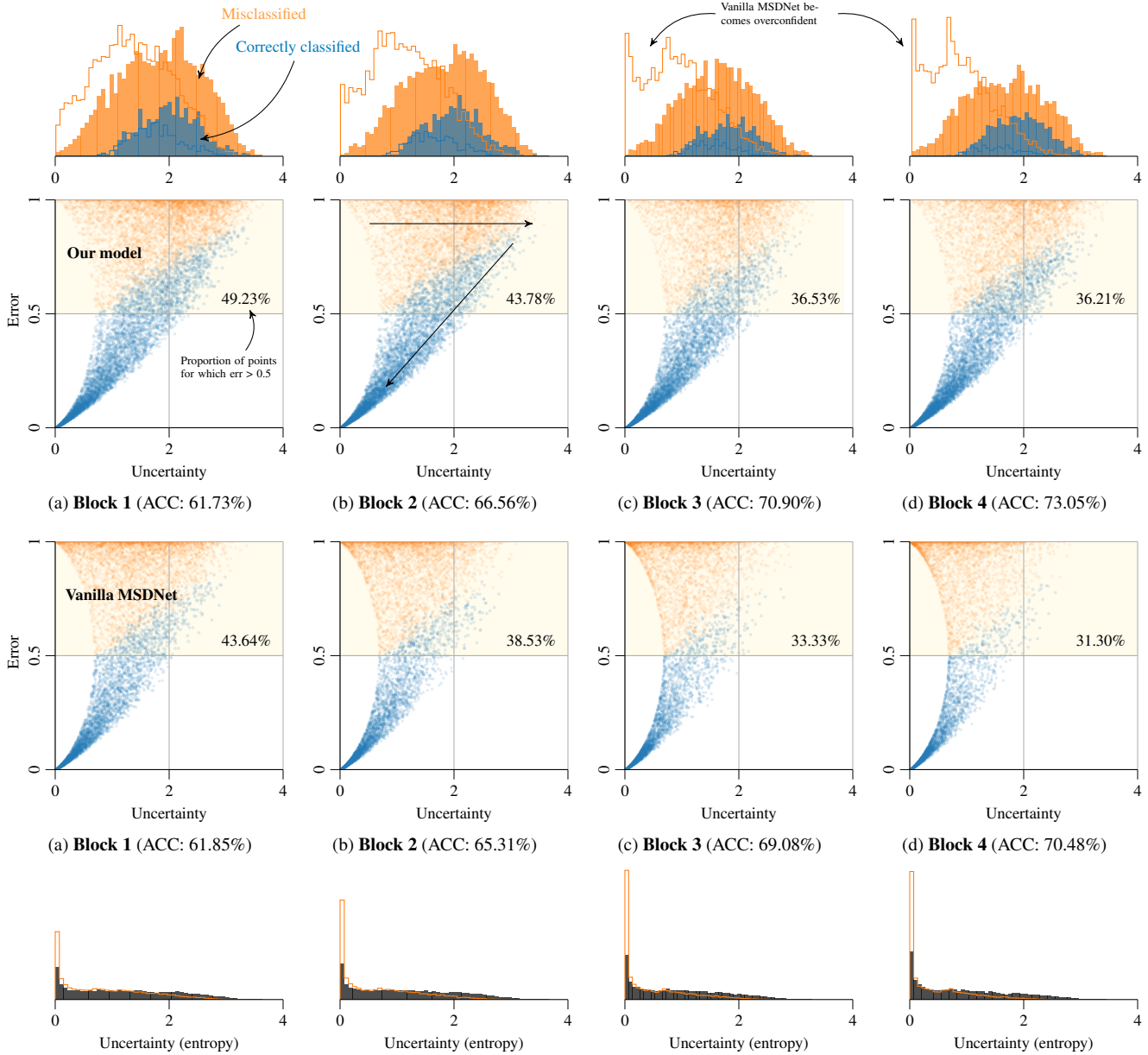


Figure 8. The second row scatter plots show \bullet correctly classified and \ast misclassified test points for our model on an uncertainty vs. error axis (repeated from Fig. 8) and the third row shows the corresponding scatter plots for the vanilla MSDNet model. The uncertainty of the points in the top half of each scatter plot is summarized as a histogram in the top row (repeated from Fig. 8). Our model result is shown in the solid histograms, while the vanilla MSDNet results are shown as a histogram outline. Uncertainty histograms of all points in the uncertainty–error scatter plots are shown in the bottom row, comparing our model (black histogram) to the vanilla MSDNet model (orange outline). We can see that the vanilla MSDNet has overall much less uncertainty in its predictions

Laplace prior variance in a grid search, or optimise neither using fixed default values. We also include an ablation result where only temperature scaling is used on the vanilla model predictions. Tab. 6 also shows results for optimising the temperature scaling parameter when using MIE but without Laplace approximation. Similarly for Caltech-256, Tab. 7 shows a more extensive version of Tab. 2.

Looking at the results in these tables, we notice that although Laplace approximation alone often slightly decreases top-1 accuracy, when used together with MIE it increases top-1 accuracy above what MIE alone would achieve, suggesting that these two methods are suitable to be used together. In Tab. 6 the result using only temperature scaling for ImageNet has identical results with the vanilla model,

Table 6. Table of Top-1/Top-5 accuracy, negative log-predictive density (NLPD), and expected calibration error (ECE) for different models on CIFAR-100 and ImageNet data. All numbers are averages over a range of computational budgets in the budgeted batch classification setup. ‘MIE Laplace $T_{\text{opt}} \sigma_{\text{opt}}$ ’-model corresponds to ‘Our model’ that is referred to in other figures. T_{opt} and σ_{opt} refer to grid search optimisation of the temperature scale and Laplace prior variance, respectively. n_{train} is the number of training samples, d is the input dimensionality, c is the number of classes, and n_{batch} is the batch size. The red and green numbers show the decrease or increase in performance compared to MSDNet (vanilla). The best performing model for each metric and each model size, on each dataset, is shown in bold.

$(n_{\text{train}}, d, c, n_{\text{batch}})$	CIFAR-100 (50000, 3072, 100, 64)				IMAGENET (1281167, 150528, 1000, 256)				
	Top-1 ACC \uparrow	Top-5 ACC \uparrow	NLPD \downarrow	ECE \downarrow	Top-1 ACC \uparrow	Top-5 ACC \uparrow	NLPD \downarrow	ECE \downarrow	
Small	MSDNet (vanilla)	69.25	90.48	1.498	0.182	68.15	88.22	1.338	0.019
	+ T_{opt}	69.06 -0.19	90.62 $+0.14$	1.207 -0.291	0.079 -0.103	68.15 $+0.00$	88.22 $+0.00$	1.338 -0.000	0.019 -0.000
	+ Laplace	69.21 -0.04	90.46 -0.02	1.419 -0.079	0.155 -0.027	68.14 -0.01	88.21 -0.01	1.335 -0.003	0.016 -0.003
	+ Laplace T_{opt}	69.02 -0.22	90.65 $+0.17$	1.196 -0.302	0.060 -0.121	68.13 -0.01	88.18 -0.04	1.337 -0.001	0.016 -0.004
	+ Laplace σ_{opt}	69.21 -0.04	90.42 -0.06	1.415 -0.082	0.154 -0.028	68.13 -0.02	88.17 -0.05	1.337 -0.001	0.016 -0.003
	+ Laplace $T_{\text{opt}} \sigma_{\text{opt}}$	69.06 -0.19	90.58 $+0.10$	1.208 -0.289	0.073 -0.109	68.10 -0.05	88.18 -0.04	1.337 -0.001	0.015 -0.005
	+ MIE	69.97 $+0.72$	90.88 $+0.40$	1.218 -0.280	0.080 -0.102	68.27 $+0.12$	88.13 -0.10	1.355 $+0.017$	0.055 $+0.036$
	+ MIE T_{opt}	69.74 $+0.50$	91.11 $+0.63$	1.133 -0.365	0.028 -0.154	68.25 $+0.10$	88.04 -0.18	1.353 $+0.015$	0.038 $+0.019$
	+ MIE Laplace	69.99 $+0.74$	90.88 $+0.40$	1.189 -0.308	0.056 -0.125	68.26 $+0.11$	88.11 -0.11	1.361 $+0.023$	0.070 $+0.051$
	+ MIE Laplace T_{opt}	69.83 $+0.58$	91.10 $+0.62$	1.135 -0.363	0.021 -0.161	68.22 $+0.07$	88.06 -0.16	1.357 $+0.019$	0.055 $+0.036$
	+ MIE Laplace σ_{opt}	69.89 $+0.64$	90.94 $+0.46$	1.192 -0.306	0.059 -0.122	68.25 $+0.10$	88.14 -0.08	1.360 $+0.022$	0.070 $+0.051$
	+ MIE Laplace $T_{\text{opt}} \sigma_{\text{opt}}$	69.84 $+0.59$	91.09 $+0.61$	1.133 -0.364	0.017 -0.165	68.31 $+0.16$	88.11 -0.11	1.356 $+0.018$	0.052 $+0.032$
Medium	MSDNet (vanilla)	74.12	91.94	1.549	0.190	72.78	91.01	1.123	0.033
	+ T_{opt}	73.96 -0.17	92.05 $+0.10$	1.063 -0.486	0.078 -0.112	72.78 -0.00	91.01 $+0.00$	1.123 $+0.000$	0.033 $+0.000$
	+ Laplace	73.96 -0.16	91.94 -0.00	1.436 -0.113	0.172 -0.018	72.69 -0.09	91.04 $+0.03$	1.117 -0.006	0.012 -0.021
	+ Laplace T_{opt}	73.98 -0.15	92.01 $+0.07$	1.056 -0.493	0.070 -0.120	72.68 -0.10	90.98 -0.03	1.117 -0.005	0.013 -0.020
	+ Laplace σ_{opt}	74.18 $+0.05$	91.85 -0.09	1.405 -0.144	0.164 -0.026	72.70 -0.08	91.00 -0.01	1.117 -0.005	0.013 -0.020
	+ Laplace $T_{\text{opt}} \sigma_{\text{opt}}$	73.92 -0.20	92.01 $+0.06$	1.070 -0.479	0.083 -0.107	72.72 -0.07	91.03 $+0.03$	1.118 -0.005	0.018 -0.015
	+ MIE	75.03 $+0.91$	92.97 $+1.03$	1.011 -0.538	0.050 -0.140	72.98 $+0.20$	91.12 $+0.11$	1.119 -0.004	0.042 $+0.009$
	+ MIE T_{opt}	74.94 $+0.82$	93.23 $+1.29$	0.941 -0.608	0.028 -0.162	72.99 $+0.21$	91.09 $+0.08$	1.119 -0.004	0.038 $+0.005$
	+ MIE Laplace	74.99 $+0.86$	93.01 $+1.07$	0.990 -0.559	0.032 -0.158	72.95 $+0.17$	91.15 $+0.14$	1.128 $+0.005$	0.065 $+0.032$
	+ MIE Laplace T_{opt}	74.96 $+0.84$	93.19 $+1.24$	0.947 -0.602	0.015 -0.175	72.88 $+0.10$	91.06 $+0.06$	1.124 $+0.001$	0.045 $+0.012$
	+ MIE Laplace σ_{opt}	75.04 $+0.92$	92.95 $+1.01$	0.989 -0.560	0.031 -0.159	72.97 $+0.19$	91.12 $+0.11$	1.126 $+0.003$	0.064 $+0.030$
	+ MIE Laplace $T_{\text{opt}} \sigma_{\text{opt}}$	74.99 $+0.86$	93.23 $+1.29$	0.944 -0.605	0.026 -0.164	73.04 $+0.26$	90.96 -0.05	1.121 -0.002	0.031 -0.003
Large	MSDNet (vanilla)	75.36	92.78	1.475	0.178	74.33	91.57	1.066	0.050
	+ T_{opt}	75.27 -0.10	92.76 -0.02	0.984 -0.491	0.059 -0.119	74.33 $+0.00$	91.57 $+0.00$	1.066 $+0.000$	0.050 $+0.000$
	+ Laplace	75.41 $+0.05$	92.76 -0.02	1.347 -0.128	0.157 -0.021	74.25 -0.08	91.55 -0.02	1.052 -0.014	0.019 -0.031
	+ Laplace T_{opt}	75.28 -0.08	92.79 $+0.01$	0.999 -0.476	0.077 -0.101	74.25 -0.08	91.55 -0.02	1.053 -0.012	0.019 -0.031
	+ Laplace σ_{opt}	75.36 -0.01	92.75 -0.04	1.338 -0.137	0.157 -0.020	74.25 -0.08	91.55 -0.03	1.053 -0.013	0.017 -0.033
	+ Laplace $T_{\text{opt}} \sigma_{\text{opt}}$	75.32 -0.05	92.83 $+0.05$	0.996 -0.479	0.075 -0.103	74.29 -0.04	91.53 -0.04	1.053 -0.013	0.020 -0.030
	+ MIE	76.32 $+0.95$	93.50 $+0.72$	0.949 -0.525	0.061 -0.117	74.82 $+0.49$	91.88 $+0.30$	1.029 -0.037	0.028 -0.022
	+ MIE T_{opt}	76.22 $+0.85$	93.75 $+0.97$	0.886 -0.589	0.032 -0.145	74.90 $+0.58$	91.87 $+0.30$	1.029 -0.037	0.022 -0.028
	+ MIE Laplace	76.43 $+1.07$	93.55 $+0.76$	0.924 -0.551	0.040 -0.137	74.76 $+0.43$	91.90 $+0.33$	1.035 -0.030	0.052 $+0.002$
	+ MIE Laplace T_{opt}	76.30 $+0.93$	93.74 $+0.96$	0.887 -0.588	0.036 -0.142	74.86 $+0.53$	91.78 $+0.21$	1.032 -0.034	0.026 -0.024
	+ MIE Laplace σ_{opt}	76.33 $+0.96$	93.54 $+0.75$	0.925 -0.550	0.043 -0.135	74.81 $+0.49$	91.87 $+0.29$	1.033 -0.032	0.050 -0.000
	+ MIE Laplace $T_{\text{opt}} \sigma_{\text{opt}}$	76.34 $+0.98$	93.84 $+1.05$	0.885 -0.590	0.025 -0.152	74.80 $+0.47$	91.81 $+0.24$	1.032 -0.034	0.032 -0.019

as the best temperature after optimization ended up being the default temperature, suggesting that the vanilla MSDNet on ImageNet is already quite well calibrated. This is reflected in the results in Tab. 6 also through the fact that our methods that attempt to improve decision-making through improved calibration, do not achieve major improvement in top-1 accuracy on ImageNet, as there is not much room to improve calibration over the vanilla MSDNet. This is likely explained by the vanilla MSDNet underfitting the ImageNet data, as even the largest MSDNet architecture we used for ImageNet is several magnitudes smaller than the state-of-the-art models. On CIFAR-100 and Caltech-256 the MSDNet models are large enough to overfit, as is usually the case for most models on most datasets, and we see considerable improvements in also top-1 accuracy.

In order to investigate the contribution of better decision-making on the improvements in the predictive performance, we performed an experiment trying to separate the improvement due to better decision-making from the improvement due to better predictions at each individual intermediate

exit of the dynamic neural network. In this experiment, we replaced the vanilla model decision-making with the decision-making of our model, while using the vanilla model predictions for calculating the results. Full results for CIFAR-100 are in Fig. 9 showing that our approach improves both decision-making (orange curve vs. light blue curve) and prediction quality (light blue curve vs. black curve). Interestingly, apart from improving accuracy, better decision-making also improves calibration and uncertainty estimates, as seen from the improved ECE and NLPD. However, this experiment is problematic in providing information on decision-making quality, as one model is making decisions using predictions from another model, potentially resulting in false interpretation of bad decision-making, if different models predict different samples correctly.

In addition to the experiments shown, we experimented using predictive variance or entropy as the uncertainty metric to make decisions on when to exit the MSDNet pipeline. In our experiments these metrics performed worse than the model predicted confidence, and hence we use model pre-

Table 7. Table of Top-1/Top-5 accuracy, NLPD, ECE for different models on Caltech-256. All numbers are averages over a range of computational budgets. ‘MIE Lap $T_{\text{opt}} \sigma_{\text{opt}}$ ’-model corresponds to ‘Our model’. T_{opt} and σ_{opt} refer to grid search optimisation of the temperature scale and Laplace prior variance, respectively. n_{train} is the number of training samples, d is the input dimensionality, c is the number of classes, and n_{batch} is the batch size. The red and green numbers show the decrease or increase in performance compared to MSDNet (vanilla). The best performing model for each metric and each model size, on each dataset, is shown in bold.

		CALTECH-256 (25607, 150528, 257, 128)			
$(n_{\text{train}}, d, c, n_{\text{batch}})$		Top-1 ACC \uparrow	Top-5 ACC \uparrow	NLPD \downarrow	ECE \downarrow
Small	MSDNet (vanilla)	61.0	78.2	2.16	0.18
	+ T_{opt}	60.8 -0.3	78.4 $+0.2$	1.84 -0.31	0.01 -0.16
	+ Lap	60.7 -0.3	78.0 -0.2	1.98 -0.18	0.06 -0.12
	+ Lap T_{opt}	60.5 -0.6	78.3 $+0.0$	1.86 -0.29	0.05 -0.13
	+ Lap σ_{opt}	60.6 -0.4	78.0 -0.2	1.99 -0.17	0.06 -0.12
	+ Lap $T_{\text{opt}} \sigma_{\text{opt}}$	60.5 -0.5	78.1 -0.1	1.86 -0.29	0.05 -0.13
	+ MIE	61.9 $+0.9$	78.8 $+0.6$	1.94 -0.21	0.08 -0.10
	+ MIE T_{opt}	61.5 $+0.5$	79.1 $+0.9$	1.79 -0.37	0.04 -0.13
	+ MIE Lap	61.8 $+0.7$	78.8 $+0.5$	1.86 -0.30	0.04 -0.14
	+ MIE Lap T_{opt}	61.5 $+0.5$	79.1 $+0.9$	1.82 -0.34	0.08 -0.10
	+ MIE Lap σ_{opt}	61.8 $+0.8$	79.0 $+0.8$	1.86 -0.30	0.03 -0.14
+ MIE Lap $T_{\text{opt}} \sigma_{\text{opt}}$	61.7 $+0.6$	79.0 $+0.8$	1.81 -0.34	0.09 -0.09	
Medium	MSDNet (vanilla)	63.8	80.2	1.98	0.17
	+ T_{opt}	63.5 -0.3	80.2 $+0.0$	1.70 -0.28	0.02 -0.15
	+ Lap	63.4 -0.4	79.4 -0.8	1.80 -0.18	0.03 -0.14
	+ Lap T_{opt}	63.3 -0.5	79.8 -0.3	1.73 -0.25	0.08 -0.09
	+ Lap σ_{opt}	63.4 -0.4	79.9 -0.3	1.79 -0.19	0.04 -0.13
	+ Lap $T_{\text{opt}} \sigma_{\text{opt}}$	63.4 -0.4	79.9 -0.3	1.74 -0.24	0.07 -0.10
	+ MIE	65.1 $+1.3$	81.4 $+1.2$	1.72 -0.26	0.08 -0.09
	+ MIE T_{opt}	64.6 $+0.9$	81.7 $+1.5$	1.61 -0.37	0.03 -0.14
	+ MIE Lap	64.9 $+1.2$	81.2 $+1.1$	1.67 -0.31	0.06 -0.11
	+ MIE Lap T_{opt}	64.5 $+0.7$	81.3 $+1.1$	1.67 -0.31	0.09 -0.08
	+ MIE Lap σ_{opt}	64.7 $+0.9$	81.2 $+1.0$	1.67 -0.31	0.04 -0.13
+ MIE Lap $T_{\text{opt}} \sigma_{\text{opt}}$	64.3 $+0.5$	81.3 $+1.1$	1.65 -0.33	0.08 -0.09	
Large	MSDNet (vanilla)	64.9	80.7	1.90	0.16
	+ T_{opt}	64.8 -0.1	80.7 -0.0	1.64 -0.26	0.03 -0.13
	+ Lap	64.3 -0.6	80.1 -0.6	1.72 -0.18	0.04 -0.12
	+ Lap T_{opt}	64.4 -0.5	80.0 -0.7	1.68 -0.22	0.07 -0.09
	+ Lap σ_{opt}	64.8 -0.1	80.1 -0.6	1.73 -0.17	0.03 -0.13
	+ Lap $T_{\text{opt}} \sigma_{\text{opt}}$	64.7 -0.2	80.7 $+0.0$	1.65 -0.25	0.04 -0.12
	+ MIE	65.9 $+0.9$	82.4 $+1.8$	1.62 -0.28	0.06 -0.10
	+ MIE T_{opt}	65.9 $+1.0$	82.5 $+1.9$	1.54 -0.36	0.04 -0.12
	+ MIE Lap	65.9 $+1.0$	82.1 $+1.5$	1.59 -0.31	0.08 -0.08
	+ MIE Lap T_{opt}	65.9 $+0.9$	82.4 $+1.8$	1.59 -0.31	0.11 -0.05
	+ MIE Lap σ_{opt}	65.9 $+0.9$	82.4 $+1.7$	1.58 -0.31	0.07 -0.09
+ MIE Lap $T_{\text{opt}} \sigma_{\text{opt}}$	65.6 $+0.7$	82.5 $+1.8$	1.58 -0.32	0.09 -0.07	

dictive confidence for decision-making in all experiments shown in this paper.

C. Analysis on Laplace Approximation and MIE Computational Cost

Using the Laplace approximation requires calculating the approximate inverse Hessians \mathbf{H}^{-1} and $\Sigma_{\mathbf{b}}$ for the last layer weights and biases respectively, for each intermediate classifier. As this can be precomputed before observing the test data, the only additional test time cost of the Laplace approximation comes from transforming the Laplace approximated distribution for the last layer weights $\mathcal{N}(\theta | \theta_{\text{MAP}}, \Sigma)$ to an output predictive distribution $p(\hat{z}_i | \mathbf{x}_i)$ and sampling from this distribution for n_{MC} times. Recall that $\hat{y}_i = \text{softmax}(\hat{z}_i)$, where $\hat{z}_i = \mathbf{W}\phi_i + \mathbf{b}$.

Naïve approach We use the KFAC approximation to the

inverse Hessian $\mathbf{H}^{-1} = \mathbf{V}^{-1} \otimes \mathbf{U}^{-1}$. Let $\mathbf{W} \in \mathbb{R}^{p \times c}$, $\mathbf{b} \in \mathbb{R}^{1 \times c}$ denote the weight matrix and bias terms of the k^{th} exit, and $\phi_i \in \mathbb{R}^p$ denote the features of input sample \mathbf{x}_i before the last linear layer of the k^{th} exit. Then the additional cost associated to a naïve implementation of the Laplace approximation at the k^{th} exit is based on

$$\hat{\mathbf{z}}_i \sim \mathcal{N}(\underbrace{\mathbf{W}_{\text{MAP}}^{\top} \phi_i + \mathbf{b}_{\text{MAP}}}_{\text{also needed for vanilla}}, \underbrace{(\phi_i^{\top} \mathbf{V} \phi_i) \mathbf{U} + \Sigma_{\mathbf{b}}}_{(p+1)(2p-1)+2c^2}) \quad (5)$$

with additional costs to compute the Cholesky factorisation ($\frac{1}{3}c^3$) and rescaling and shifting the samples drawn from a standard normal, resulting in a total of

$$\text{FLOPs}_{\text{naïve}} = 2c^2(n_{\text{MC}} + 1) + \frac{1}{3}c^3 + 2p^2 + p - 1. \quad (6)$$

additional FLOPs. The calculation of the mean in Eq. (5) does not add computation as this operation is also performed to obtain the vanilla MSDNet prediction. The cubic scaling of FLOPs with the number of classes is what makes the naïve approach prohibitively expensive to be viable in the budget restricted regime if the number of classes is large. The Cholesky factorization of the covariance matrix that is required for sampling can not be pre-computed before test time as the covariance matrix $(\phi_i^{\top} \mathbf{V} \phi_i) \mathbf{U} + \Sigma_{\mathbf{b}}$ depends on the test samples.

Efficient approach Sampling from the Laplace predictive distribution can be made more efficient by absorbing the bias terms into the weight matrix, *i.e.*, $\hat{\mathbf{W}} \in \mathbb{R}^{(p+1) \times c}$. This appends an additional dimension to ϕ and \mathbf{V} which we now denote by $\hat{\phi} = (\phi^{\top}, 1)^{\top}$ and $\hat{\mathbf{V}}$, respectively. Now, the output predictive distribution takes the form $\hat{\mathbf{z}}_i \sim \mathcal{N}(\hat{\mathbf{W}}_{\text{MAP}}^{\top} \hat{\phi}_i, (\hat{\phi}_i^{\top} \hat{\mathbf{V}} \hat{\phi}_i) \mathbf{U})$, which means that the costly operations can all be pre-computed offline. Most notably, although the covariance matrix $(\hat{\phi}_i^{\top} \hat{\mathbf{V}} \hat{\phi}_i) \mathbf{U}$ still depends on the test samples, the test sample dependent term $\hat{\phi}_i^{\top} \hat{\mathbf{V}} \hat{\phi}_i$ is a scalar and can be taken out of the costly Cholesky factorization, which allows performing this on the matrix \mathbf{U} before test time. This means that for one MC sample l , the pre-softmax output can be evaluated as

$$\hat{\mathbf{z}}_i^{(l)} = \underbrace{\hat{\mathbf{W}}_{\text{MAP}}^{\top} \hat{\phi}_i}_{\text{also needed for vanilla}} + \underbrace{\sqrt{\hat{\phi}_i^{\top} \hat{\mathbf{V}} \hat{\phi}_i}}_{(p+2)(2p+1)} \underbrace{(\mathbf{L} \mathbf{g}^{(l)})}_{2c^2 - c}, \quad (7)$$

where $\mathbf{g}^{(l)} \sim \mathcal{N}(\mathbf{0}, \mathbf{I})$ and \mathbf{L} is the pre-calculated Cholesky factor of \mathbf{U} . Even the samples $\mathbf{g}^{(l)}$ can be pre-drawn and pre-multiplied with \mathbf{L} , which further reduces the computational cost to

$$\text{FLOPs}_{\text{efficient}} = 2cn_{\text{MC}} + 2p^2 + 5p + 2. \quad (8)$$

Based on this analysis, Fig. 10 shows the incremental test time computational cost of applying Laplace approximation on top of the vanilla MSDNet model for CIFAR-100,

Table 8. Table of Top-1/Top-5 accuracy, negative log-predictive density (NLPD), and expected calibration error (ECE) for different models on CIFAR-100. ‘Our model’ corresponds to ‘MIE Laplace $T_{\text{opt}} \sigma_{\text{opt}}$ ’-model in other result tables. These results show a decision-making experiment, where vanilla MSDNet and ‘Our model’ results are compared to results obtained by using a setup where our model is used for decision-making, and predictions are from vanilla MSDNet. The best-performing model for each metric and each model size is shown in bold.

$(n_{\text{train}}, d, c, n_{\text{batch}})$		CIFAR-100 (50000, 3072, 100, 64)			
		Top-1 ACC \uparrow	Top-5 ACC \uparrow	NLPD \downarrow	ECE \downarrow
Small	MSDNet (vanilla)	69.25	90.48	1.498	0.182
	Vanilla predictions, our model decisions	69.33 $+0.09$	90.60 $+0.12$	1.300 -0.197	0.108 -0.074
	Our model	69.84 $+0.59$	91.09 $+0.61$	1.133 -0.364	0.017 -0.165
Medium	MSDNet (vanilla)	74.12	91.94	1.549	0.190
	Vanilla predictions, our model decisions	74.51 $+0.39$	92.20 $+0.25$	1.460 -0.089	0.168 -0.022
	Our model	74.99 $+0.86$	93.23 $+1.29$	0.944 -0.605	0.026 -0.164
Large	MSDNet (vanilla)	75.36	92.78	1.475	0.178
	Vanilla predictions, our model decisions	75.72 $+0.36$	92.71 -0.08	1.388 -0.086	0.162 -0.015
	Our model	76.34 $+0.98$	93.84 $+1.05$	0.885 -0.590	0.025 -0.152

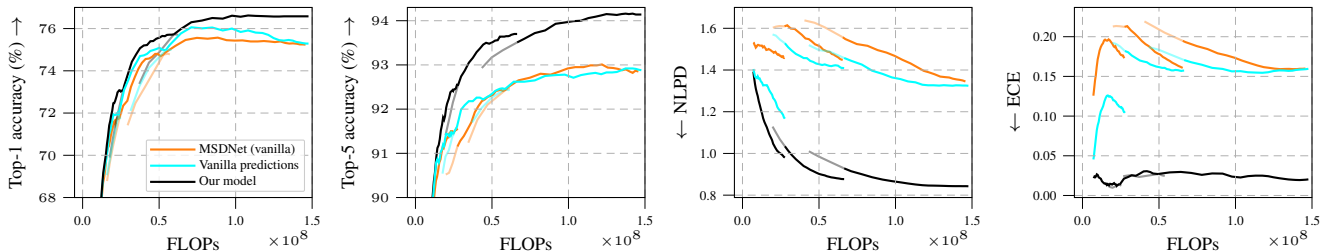


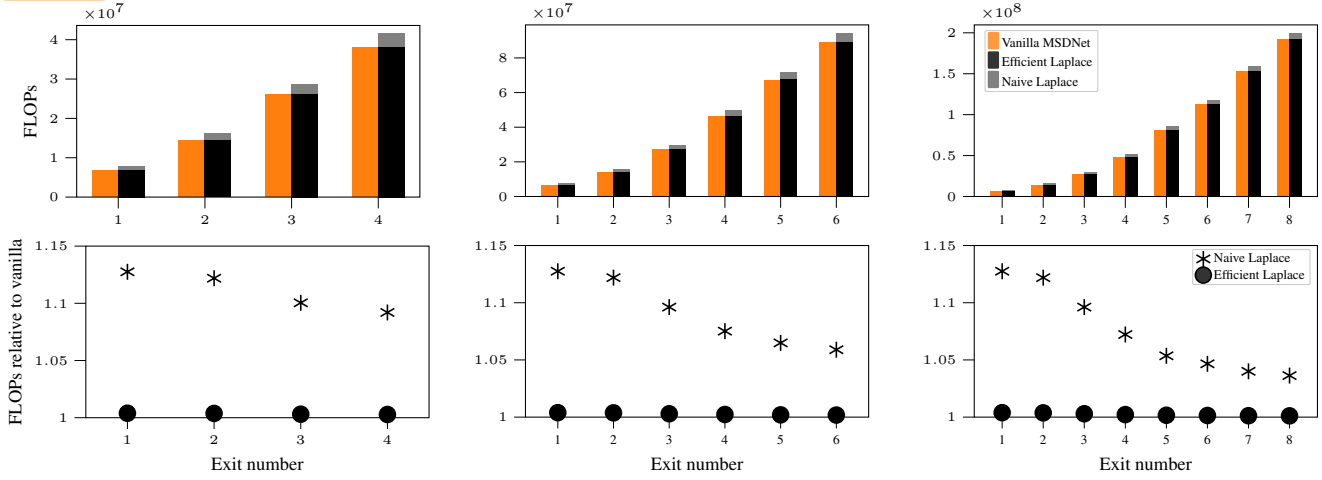
Figure 9. Accuracy (Top-1 & Top-5) and uncertainty metrics (NLPD and ECE) on a budgeted batch classification task as a function of average computational budget per image (FLOPs) on the CIFAR-100 data set with a small/medium/large model. These results show a decision-making experiment, where vanilla MSDNet and ‘Our model’ results are compared to results obtained by using a setup where our model is used for decision-making, and predictions are from vanilla MSDNet (labelled ‘Vanilla predictions’).

ImageNet, and Caltech-256, showing the increase in computation both for the efficient sampling approach and for the naïve sampling approach. For all data sets the small, medium, and large models are analysed separately, and for each model, the increase in computational cost at each intermediate exit is shown. The calculation of FLOPs in these figures differs from what is shown in the formulas above, as the FLOPs in the figure results are ‘practical FLOPs’ that take into account the ability of most hardware to calculate sequential multiplication and addition in a single operation, resulting in one FLOP instead of two for such a pair of operations. Practical FLOPs are used also for the FLOPs calculation of all other numerical results in this paper. The results of the figure are obtained considering that 50 MC samples are drawn from the Laplace approximated predictive output distribution. The figures show that naïve approach of Laplace approximation adds considerable computation, but this can be mitigated by using the efficient sampling approach. The remaining added computational cost of efficient Laplace that is hard to see in Fig. 10 is 0.1–0.4% on CIFAR-100, 0.06–0.16% on ImageNet, and 0.04–0.15% on Caltech-256 depending on the exit used. As a comparison, using a last layer MC dropout with 50 samples would add

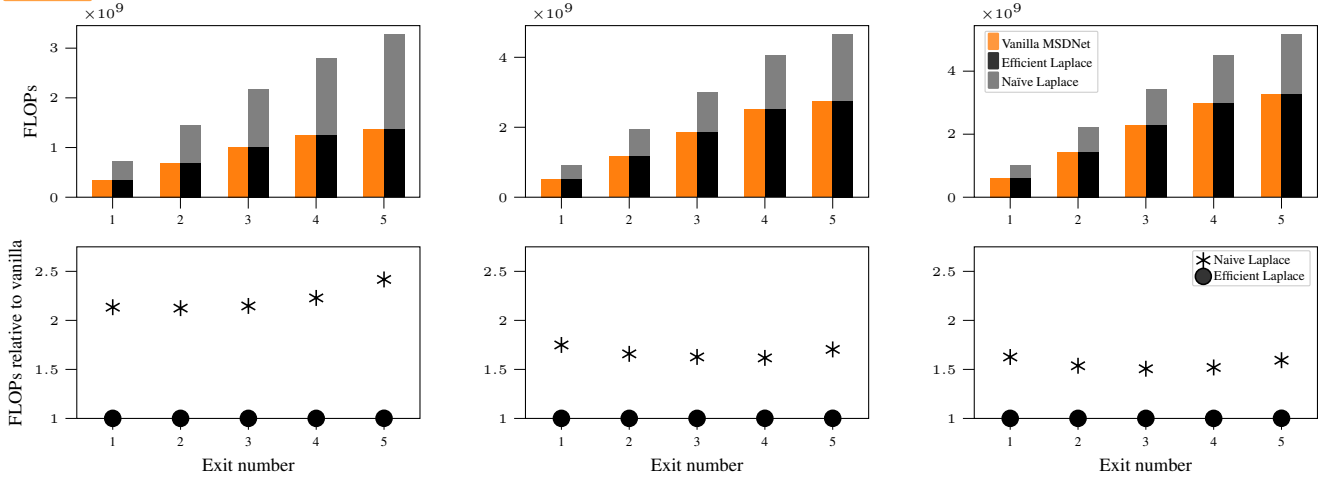
3–9% computation on CIFAR-100, 4–10% on ImageNet, and 1–3% on Caltech-256.

Using MIE adds even less computation compared to our efficient Laplace. At each exit apart from the first one, the c dimensional output is multiplied by the weight averaging weight w_k , added to the cumulative total sum, which is then divided by the total weight $\sum_{j=1}^k w_j$, adding up to $3c$ additional FLOPs at each exit after the first one. This results to additional 0.001–0.002% computation on CIFAR-100, 0.0002–0.0009% on ImageNet, and 0.0001–0.0002% on Caltech-256.

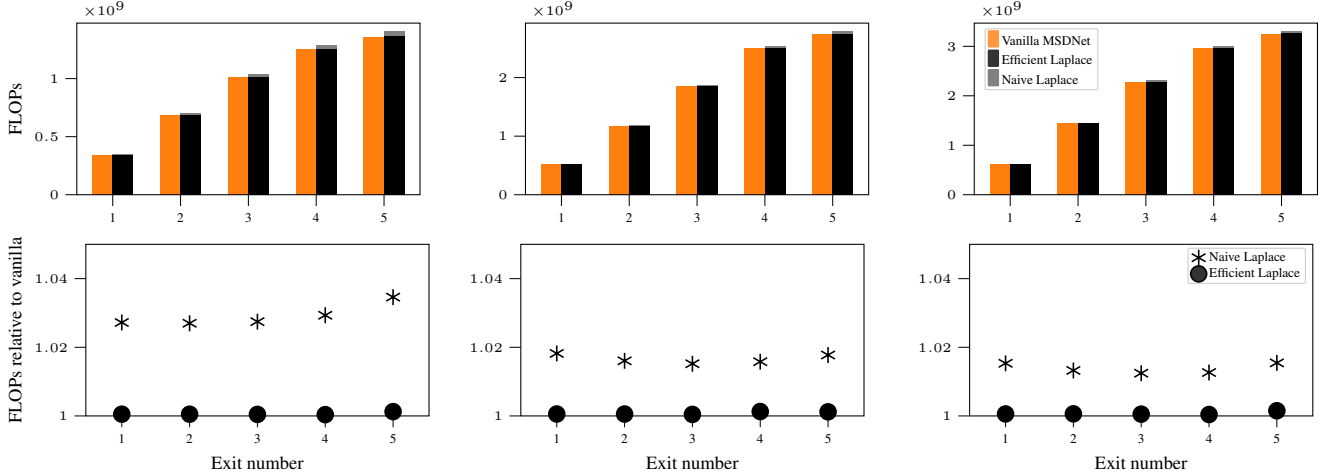
CIFAR-100



ImageNet



Caltech-256



(a) small models

(b) medium models

(c) large models

Figure 10. Analysis on the test time computational cost of the Laplace approximation for different models. First rows show bar graphs comparing the computational costs of vanilla MSDNet (orange) and MSDNet with Laplace approximation (black) at each intermediate exit. The solid black bars represent the computational cost of efficient sampling from the predictive distribution, while the grey bars show the cost of naïve sampling. The second rows show the relative computational cost of using Laplace approximation on top of the vanilla MSDNet, both for the efficient and the naïve sampling approach. The figures assume 50 MC samples are drawn from the predictive distribution.